AFRL-VS-TR-2002-1586

Observations and Modeling of Atmospheric Radiance Structure

Peter P. Wintersteiner

ARCON Corporation
260 Bear Hill Rd.
Waltham, MA 02451-1080

November 2001

Final Report

APPROVED FOR PUBLIC RELEASE; DISTRIBUTION IS UNLIMITED.

AIR FORCE RESEARCH LABORATORY
Space Vehicles Directorate
29 Randolph Rd
AIR FORCE MATERIEL COMMAND
Hanscom AFB, MA 01731-3010

20030107 041

This technical report has been reviewed and is approved for publication.

for DEAN KIMBALL
Contract Manager

GERALD J. ZDYB, Deputy Chief
Space Based Infrared Technology
Center of Excellence
Space Vehicles Directorate

This report has been reviewed by the ESC Public Affairs Office (PA) and is releasable to the National Technical Information Service (NTIS).

Qualified requestors may obtain additional copies from the Defense Technical Information Center (DTIC). All others should apply to the National Technical Information Service (NTIS).

If your address has changed, if you which to be removed from the mailing list, or if the addressee is no longer employed by your organization, please notify AFRL/VSIM, 29 Randolph Road, Hanscom AFB MA 01731-3010. This will assist us in maintaining a current mailing list.

Do not return copies of this report unless contractual obligations or notices on a specific document require that it be returned.

REPORT DOCUMENTATION PAGE

Form Approved
OMB NO. 0704-0188

Public Reporting burden for this collection of information is estimated to average 1 hour per response, including the time for reviewing instructions, searching existing data sources, gathering and maintaining the data needed, and completing and reviewing the collection of information. Send comment regarding this burden estimates or any other aspect of this collection of information, including suggestions for reducing this burden, to Washington Headquarters Services, Directorate for information Operations and Reports, 1215 Jefferson Davis Highway, Suite 1204, Arlington, VA 22202-4302, and to the Office of Management and Budget, Paperwork Reduction Project (0704-0188,) Washington, DC 20503.

1. AGENCY USE ONLY (Leave Blank)

2. REPORT DATE
9 November 2001

3. REPORT TYPE AND DATES COVERED
Final Report

4. TITLE AND SUBTITLE
Observations and Modeling of Atmospheric Radiance Structure

5. FUNDING NUMBERS
F19628-96-C-0048
PE: 61102F
PR: 2310
TA: GD
WU: AP

6. AUTHOR(S)
Peter P. Wintersteiner

7. PERFORMING ORGANIZATION NAME(S) AND ADDRESS(ES)
ARCON Corporation
260 Bear Hill Rd.
Waltham, MA, 02451-1080

8. PERFORMING ORGANIZATION REPORT NUMBER

9. SPONSORING / MONITORING AGENCY (S) NAME AND ADDRESS(ES)
Air Force Research Laboratory/VSSS
29 Randolph Rd., Hanscom AFB, MA 01731-3010
Contract Manager: Dean Kimball

10. SPONSORING / MONITORING AGENCY REPORT NUMBER
AFRL-VS-TR-2002-1586

11. SUPPLEMENTARY NOTES

12 a. DISTRIBUTION / AVAILABILITY STATEMENT
Approved for public release; Distribution Unlimited

12 b. DISTRIBUTION CODE

13. ABSTRACT (Maximum 200 words)

Several investigations related to atmospheric radiance structure have been carried out. We used auroral data from the MSX UVISI Spectrographic Imagers in the EUV, visible, and NIR wavelengths to demonstrate the excellent spatial and temporal resolution of those instruments, and their utility for studying radiance structure. We identified small perturbations in the 4.3 μm below-the-horizon data from the MSX SPIRIT III radiometer as originating in the stratosphere, helping to confirm that the structure was produced by upwelling thunderstorm-produced gravity waves. We derived and implemented a new transfer-function algorithm in Atmospheric Radiance Code (ARC), and demonstrated its functionality. It enables rapid and repetitive non-LTE calculations to be carried out, which is essential for forward modeling of radiance structure. We participated in the development of the first non-LTE kinetic temperature retrieval algorithm, which will be useful for returning profiles above 100 km using data from the SABER instrument aboard NASA's TIMED satellite, and we used ARC for related model development and validation purposes.

14. SUBJECT TERMS
Atmospheric radiance structure; Visible & infrared; CO_2 15 μm & 4.3 μm emission; non-LTE; ARC; Gravity waves; MSX; UVISI; SPIMs; SABER; Temperature retrieval; Laser bands

15. NUMBER OF PAGES

16. PRICE CODE

17.SECURITY CLASSIFICATION OF REPORT	18.SECURITY CLASSIFICATION OF THIS PAGE	19.SECURITY CLASSIFICATION OF ABSTRACT	20.LIMITATION OF ABSTRACT
Unclassified	Unclassified	Unclassified	Unlimited

Table of Contents

	Page
1. Introduction	1
2. MSX	2
2.1 UVISI SPIMs	2
2.1.1 Instruments	2
2.1.2 Data Processing	3
2.1.3 Case Study	3
2.2 Observation of Stratospheric Waves	12
3. ARC Transfer Functions	14
3.1 Introduction	14
3.2 Formulation	15
3.3 Convergence	19
3.4 Application of Stored Transfer Functions	23
4. SABER	31
4.1 Temperature Retrieval	31
4.2 Laser Bands in the Daytime CO_2 Model	35
5. Summary	38
6. References	39
Appendix A	41
Appendix B	46

1. Introduction

ARCON Corporation is pleased to submit the following Final Report, which describes the research that has been carried out under the provisions of contract # F19628-96-C-0048. There are sections summarizing work we did on (1) the Midcourse Space Experiment (MSX) project; (2) the non-LTE Atmospheric Radiance Code (ARC) that we have developed; and (3) the Sounding of the Atmosphere using Broadband Emission Radiometry (SABER) instrument.

The overall purpose of the work that we have undertaken is to provide new capabilities for observing and modeling structured radiance in the atmosphere, particularly the non-LTE regions of the atmosphere. This purpose is well served by the work reported below. It is supplemented by the transition of some of our modeling and simulation capabilities to the Air Force, in the form of codes that we have developed and advice or assistance related to their use.

Our report is accompanied by reprints of two papers that were published in *Geophysical Research Letters* during the performance period for this contract, which was from April 4, 1996 until December 31, 2000. The first of these has to do with radiance structure in MSX radiometer data, structure that has been identified with atmospheric gravity waves in the stratosphere. This is included as Appendix A. The other has to do with the principal objective of our work on the SABER project, which was the development of a non-LTE retrieval algorithm for atmospheric kinetic temperature and pressure using 15 μm emissions from CO_2. That paper comprises Appendix B. The work described in each of them is outlined in this report in summary form, whereas the remaining projects are described in somewhat more detail.

All the work reported in this document was performed by the principal author. Additional work that was reported in a Scientific Report we submitted in 1998 is not reviewed here.

2. MSX

Midcourse Space Experiment [*Mill et al, 1994*] was a satellite program designed to satisfy several DoD requirements. Among them was a requirement to produce a high-quality database of global atmospheric radiance measurements spanning the spectral range from the EUV to the LWIR, from approximately 110 to 25,000 nm. The satellite was launched in April 1996, and operated successfully until February 1997 when the solid-hydrogen cryogen expired and the infrared sensors became useless. Data were taken in a variety of limb-scanning (above the horizon, ATH) modes, and also looking downwards (below the horizon, BTH) through the atmosphere at the Earth.

The optical instruments on MSX with which we are concerned are SPatial InfraRed Imaging Telescope (SPIRIT III) and Ultraviolet/Visible Imagers and Spectrographic Imagers (UVISI). SPIRIT III consisted of an interferometer with a broad spectral range and a radiometer with five channels, including two detecting CO_2 emissions at 4.3 μm (band B) and 15 μm (band D). UVISI consisted of a suite of four 256x256 pixel imagers sensitive in the UV and visible wavelengths, and five spectrographic imagers (SPIMs) that covered the range 110 to 900 nm. Details relating to the instruments are given by Mill et al [*1994*].

Numerous publications and presentations have given examples of MSX data and discussed conclusions that have been drawn from them. We confine our discussion to those directly involving us. During the performance period for this contract, we were part of the Earthlimb Backgrounds team. Our role in the MSX program involved the collection, display, and interpretation of SPIM data, and modeling and analysis of radiometer data, principally from Bands B and D.

2.1 UVISI SPIMs

2.1.1 Instruments

Each UVISI spectrographic imager, having a dispersive grating to provide the wavelength discrimination and reflective optics to focus light passing through a horizontally-oriented slit, acquired sets of UV, visible, or NIR data with a 40x272 array of CCD detectors. Counts were binned electronically into spectra consisting of 272, 136, or 68 points. 40, 20, 10, or 5 such spectra, each slightly offset from the other in the horizontal direction (along the slit), were obtained simultaneously. The frame rate was either 2 or 4 Hz, so as many as 40 spectra were obtained every 250 or 500 ms throughout each data collect. Spectral images with a second spatial dimension, this one the vertical dimension, were assembled by use of a moving mirror that scanned upward and then downward through a range of discrete positions, providing lines of sight (LOS) corresponding to specific tangent heights. Therefore, every 5 to 30 seconds (depending on the number of mirror positions and the acquisition rate) spectra were obtained in an array covering horizontal and tangent-height distances of about 52 by 58 km, respectively, at the tangent point. In the example discussed below, a 20 by 20 image was obtained every 5 seconds, with a spatial resolution better than 3 by 3 km at the tangent point. (Due to the motion of the spacecraft, the object points are actually horizontally offset from one frame to the next, so each image would be more accurately presented as a parallelogram than as a square.)

2.1.2 Data Processing

When MSX first flew, we generated SPIM spectra for several data collection events (DCEs). We then developed several processing codes for extracting and formatting data comprising specific features in the spectra. We had defined approximately 20 so-called "sub-bands" for each SPIM. These were spectral regions, quite narrow in many cases, spanning the more important UV, visible, and NIR emission features. For example, there were two sub-bands for LBH bands, and two more for the N_2^+ First Negative emission at 391.4 nm and 427.8 nm. The Level 3 files contained "sub-band radiances", which are simply the spectral limb radiance integrated over these ranges. They were available for every super-pixel of every frame of each DCE, and when properly assimilated (and, in some cases, averaged), they provided a means of visualizing the data and studying the processes responsible for dayglow or nightglow, with excellent spatial and temporal resolution.

The data processing codes that we developed were either for extracting and storing the SPIM spectra or for manipulating the sub-band radiances. A list and a brief description of the more important ones are given below. SPIMDRVR is the processing code that produces the Level 3 files from the Level 2 files, which in turn would be produced by UVISI CONVERT.

GET_SPEC is a module for obtaining SPIM spectra from the Level 2 data files. The SPIMDRVR spectral contents file (SCF) is needed to run this code, which extracts either individual spectra (for a particular spatial pixel) or all the spectra in a given frame and writes them to an ASCII file.

ORG_SPEC is a module that stores and accesses any collection of SPIM spectra extracted from Level 2 files by GET_SPEC. It creates a searchable database, stores the data in an efficient binary format, and retrieves the spectra again as ASCII data, either individual spectra or a set of co-added spectra.

PROC_SUBB is the main module for processing sub-band radiances. It requires the radiance scan table and spectral contents files from SPIMDRVR. It writes a so-called "scan summary file", organizing the DCE segment in question into complete scans, and then writes whatever output files are requested. The possibilities, for any sub-band, are (1) radiance scan data [organized as mirror position vs scan for the entire segment]; (2) concatenated spatial images [radiance organized as spatial pixel vs tangent height for individual scans]; (3) time series [radiances for certain tangent-height bins vs time for the entire segment]; and (4) "image" files [radiances for all tangent-height bins vs scan for the entire segment]. Except for the spatial images, the sub-band radiances may be retrieved from an individual spatial pixel, or averaged over some or all of the spatial pixels.

CONC_TSR and CONC_IMG are modules for concatenating the time series and image file outputs for different segments of the same DCE.

2.1.3. Case Study

Among the DCEs that we studied, we choose EL15050000301 as a case study to illustrate the quality of the SPIM data and the results we obtained with our data processing programs. This was an auroral experiment, looking at tangent heights between 80 and 140 km as the spacecraft traversed the northern polar region on November 10, 1996. As

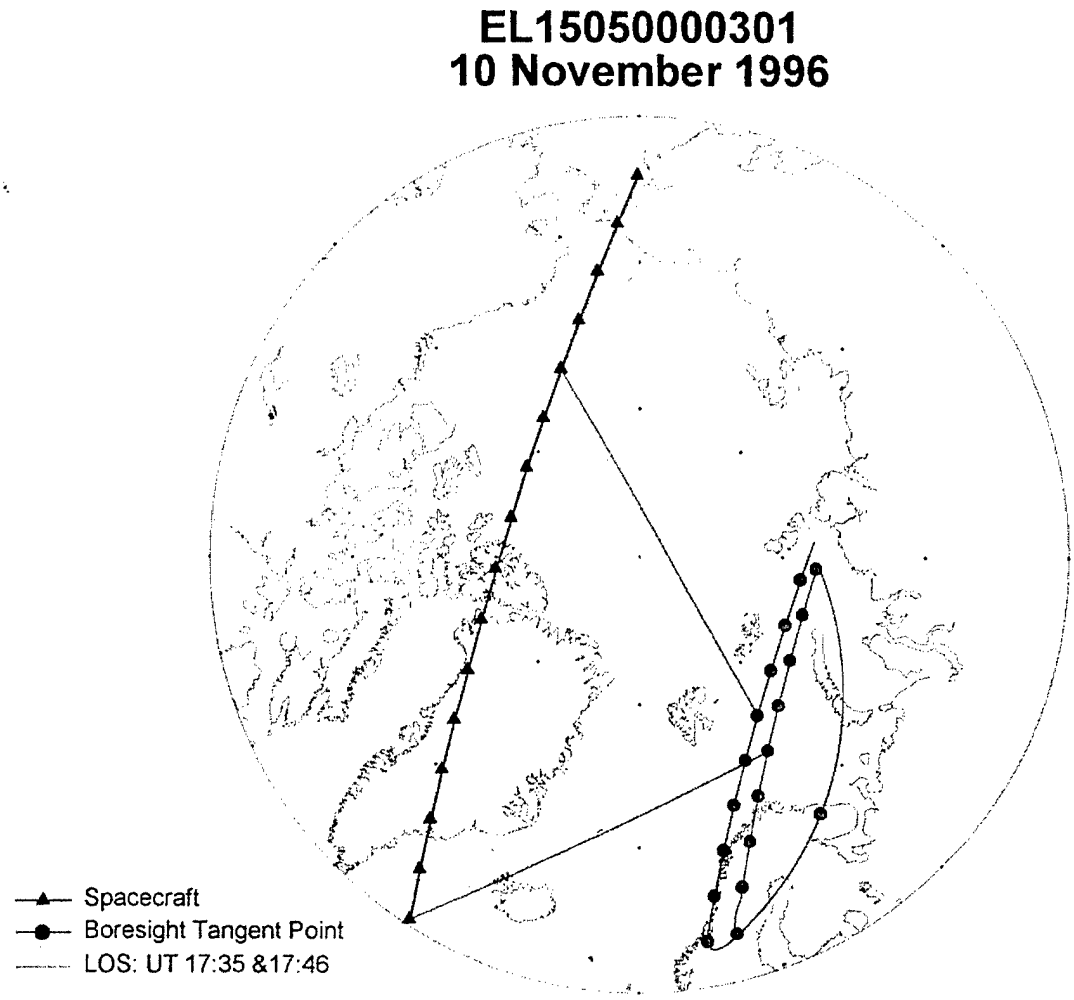

Figure 1. Location of the MSX spacecraft (blue), the locus of boresight tangent points (red) and two representative lines of sight (green) during Earthlimb experiment EL15050000301 on 10 November 1996. Triangles locate the spacecraft at one-minute intervals, starting at UT 17:35 as it approached Greenland. Circles denote the tangent points, starting at UT 17:31 over Sweden. The change in the view azimuth at about UT 17:40 (the "swingback") allowed the instruments to view the same regions twice.

shown in Figure 1, the view was over Norway and the Arctic Ocean north of Siberia. The locations of the boresight tangent point at one minute intervals starting (over Sweden) at UT 17:31 and ending at UT 17:49 are given in red. The experiment included a "swingback"; as a result, nearly the same region of space was viewed twice during separate parts of the DCE, and features that remained stationary were viewed two times, approximately 11 minutes apart, albeit from different azimuth angles. This is illustrated schematically in the figure by the two lines drawn in green, which would intersect if they were extended beyond their respective tangent points.

Figure 2 shows combined spectra from SPIMs 3 through 5, covering the spectral range 260-870 nm. These come from the region of maximum dosing seen during this DCE,

which occurred just north of the North Cape of Norway. Spectra corresponding to selected tangent heights between 88 and 124 km are plotted. These spectra have been averaged over the slit. This has the effect of slightly improving the signal to noise, but the individual spectra are also excellent.

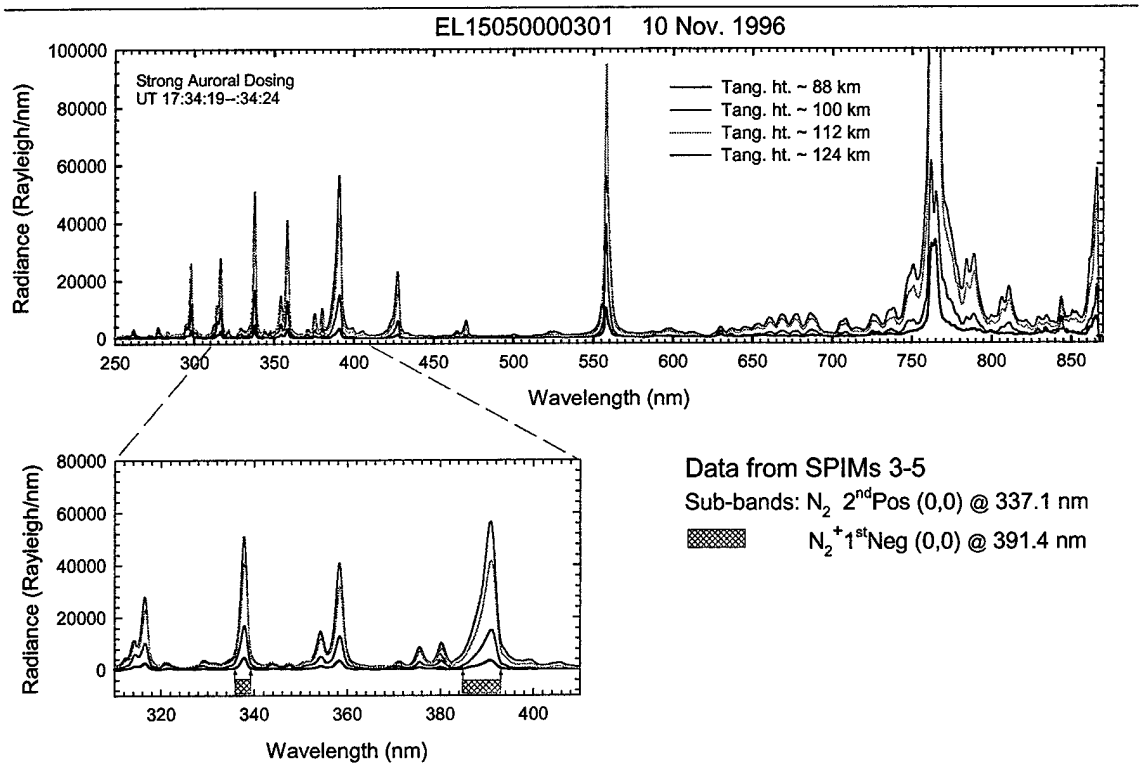

Figure 2. SPIM spectra for limb views in the MLT region, from the auroral DCE of 10 November 1996. The blowup shows the NUV region, with two sub-bands highlighted.

Many auroral emission features can be clearly seen in the combined spectrum. Peaks due to the atomic oxygen green line at 557.7 nm, the N_2^+ 1st Negative bands at 391.4, 427.8, and 470 nm, the N_2 1st Positive bands between 640 and 700 nm, and the O_2 Atmospheric Band at 762 nm stand out. Even the atomic oxygen red line at 630 nm can be discerned in these relatively low-altitude scans. In the blowup of the 310-410 nm region at the bottom, the characteristic shape of N_2^+ 1st Negative ($\Delta v=0$) bands is well resolved. Most of the other large peaks are due to the N_2 2nd Positive bands, including (0,0) at 337.1 nm. Smaller peaks can be unambiguously associated with N_2 Vegard-Kaplan bands, and there is even a small bump at 346.6 nm from an atomic oxygen line. Cross-hatched rectangles indicate the spectral region covered by two of the sub-bands selected for analysis.

Figure 3 shows combined UV spectra from SPIMs 1 and 2, with a portion from SPIM 3 included as well. These spectra were obtained from the same frames as those in Figure 2. The most prominent emission seen here is Lyman α at 121.6 nm. The blowup at the bottom left contains the atomic oxygen lines at 130.4 and 135.6 nm, as well as two LBH bands. The other blown-up region contains mostly LBH. Short-wave of Lyman α are sev-

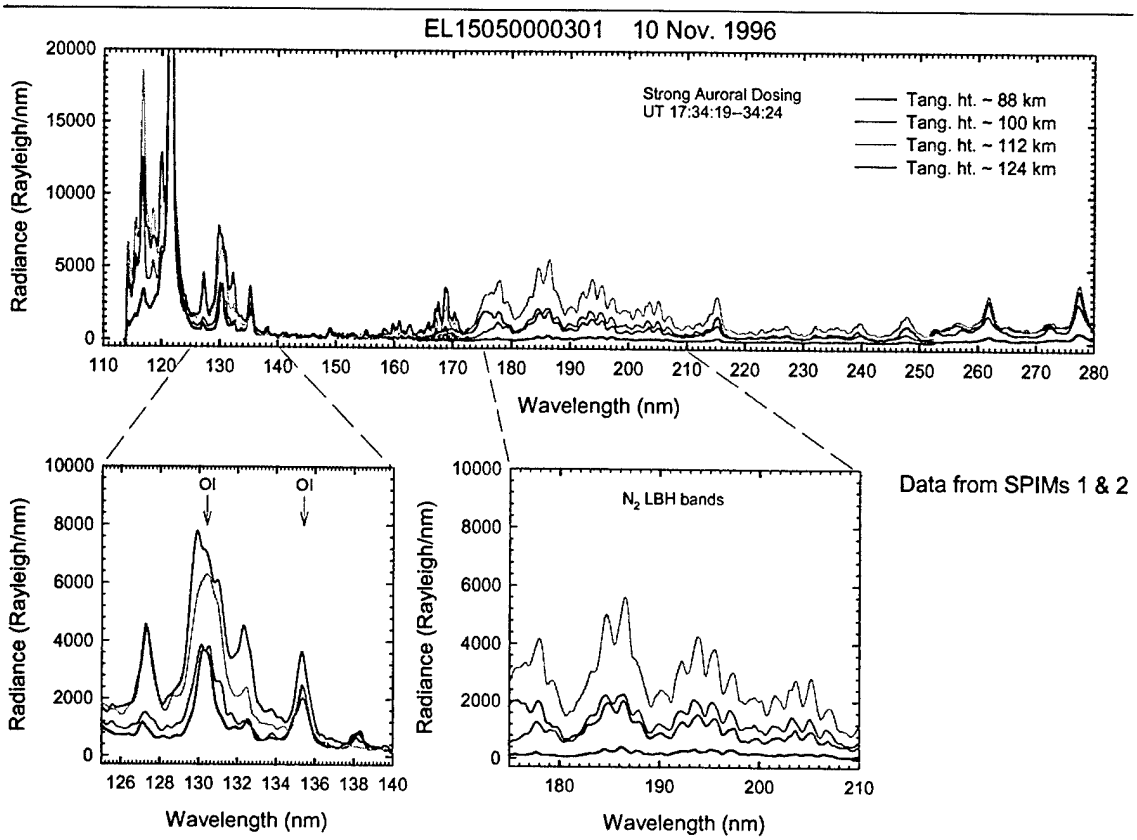

Figure 3. Auroral UV spectra. Blowups show atomic oxygen lines (left) and N_2 LBH bands (right).

eral prominent emissions, among them lines of atomic nitrogen at 117 and 120 nm. As with the spectra in Figure 2, these have been averaged over the slit.

In order to take a broader view, we assembled sub-band radiance data for the full range of tangent heights and the full (nearly 20-minute) duration of the DCE. Figure 4a shows such an overview as seen in the 391.4 nm emission, one of the standard indicators of auroral energy deposition. The intensity of this feature is plotted in false color against tangent height on the vertical axis and time on the horizontal axis. Regions of black indicate absence of data, for example where the tangent height was greatly elevated during the swingback near 17:40 UT, or to very low emission rates as seen near 17:44. The first couple of minutes, on the left, show no indication of auroral activity. There is a brief surge near 17:33, but the brightest emission occurs after 17:34 when the tangent point is over the North Cape. Immediately after this time, the emission appears to come from successively lower altitudes, which is an indication that the dosing region was well away from the tangent point. Auroral activity is evident for several minutes thereafter. The bright spot at about 17:45 corresponds to lines of sight traversing the region seen earlier at 17:34.

Figures 4b and 4c give the same information, but for the atomic oxygen emission at 557.7 nm and the N_2 2nd Positive emission at 337.1 nm. The patterns are very nearly the

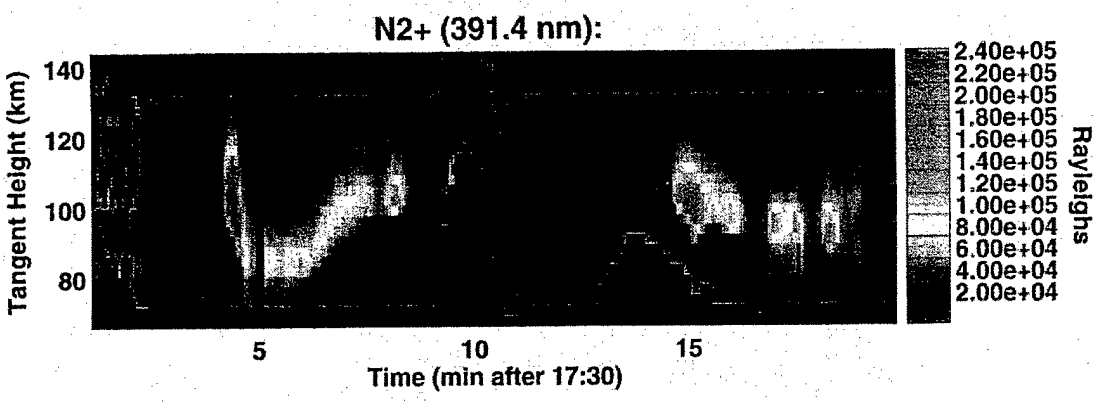

Figure 4a. Overview of EL15050000301, as seen in the N_2^+ emission at 391.4 nm.

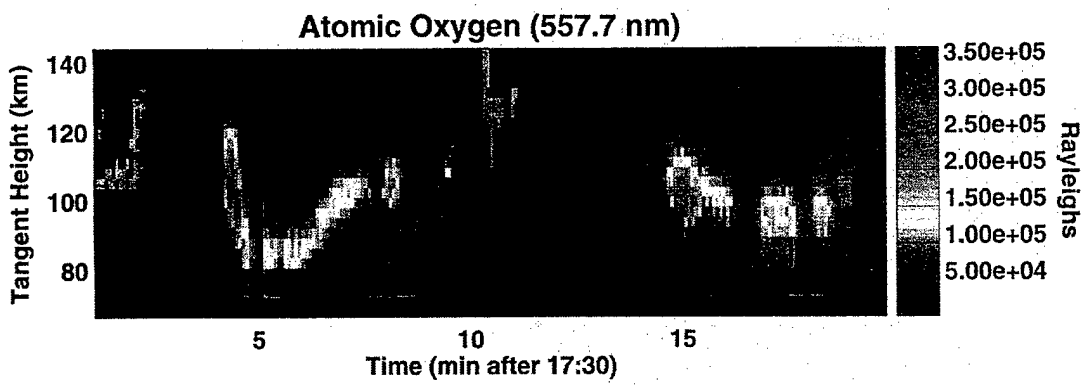

Figure 4b. Overview of EL15050000301 as seen in the OI emission at 557.7 nm.

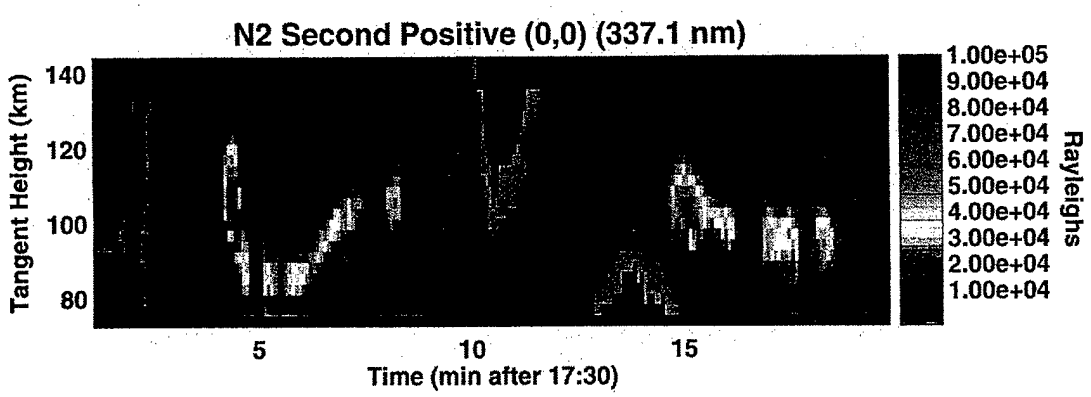

Figure 4c. Overview of EL15050000301 as seen in the N_2 emission at 337.1 nm.

same as those in Figure 3a, which is expected since electron-impact excitation of the emitting states is the driving mechanism in all cases. At the beginning of the DCE one can also see some green line near 93 km, as expected for undisturbed nighttime conditions. The peak intensities recorded in Figures 4a-4c are approximately 300 kR, 450 kR, and 100 kR respectively. The emission ratios appear to be invariant over a large range of tangent heights and dosing strengths. We find that the 391.4/557.7 ratio is about 1:1.6, and the 337.1/391.4 ratio is about 1:2.2.

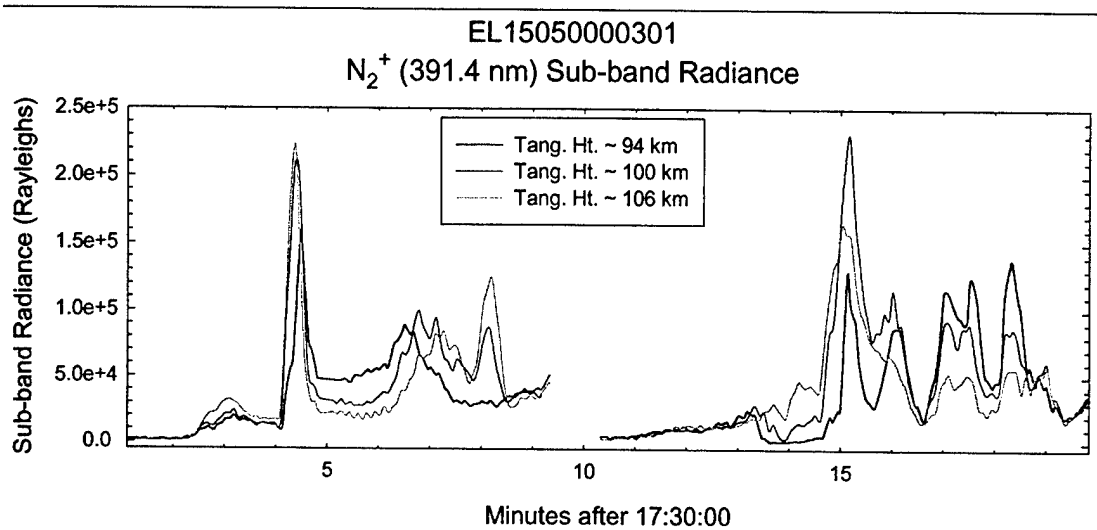

Figure 5. Time series of N_2^+ emission at 391.4 nm, for selected tangent heights, during EL15050000301

Figure 5 shows a slice of 391.4 nm data from particular tangent heights near altitudes where the maximum dosing occurred, as a function of time. The rapid onset of activity is evident near 17:34, and the same level of brightness is achieved 11 minutes later after the swingback.

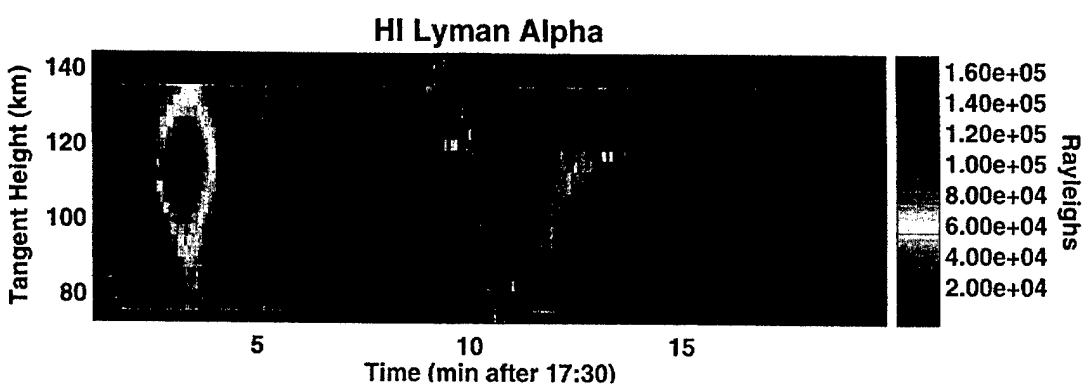

Figure 6. Overview of EL15050000301 as seen in the Lyman α emission at 121.6 nm.

The image of Lyman α emissions at 121.6 nm that is recorded as Figure 6 is not similar to the three images in Figure 4 at all, indicating that proton and electron precipitation patterns were quite different. In particular, the proton aurora was at its strongest near 17:33 UT and so appears at the southern edge of the dosing region (see Figure 1), whereas its intensity was greatly diminished in the places where the electron precipitation was the greatest. Also, the much weaker peak that is visible after the swingback came at about 17:42, nine minutes after the first peak, showing that the proton precipitation had not only diminished in intensity but had also moved further South.

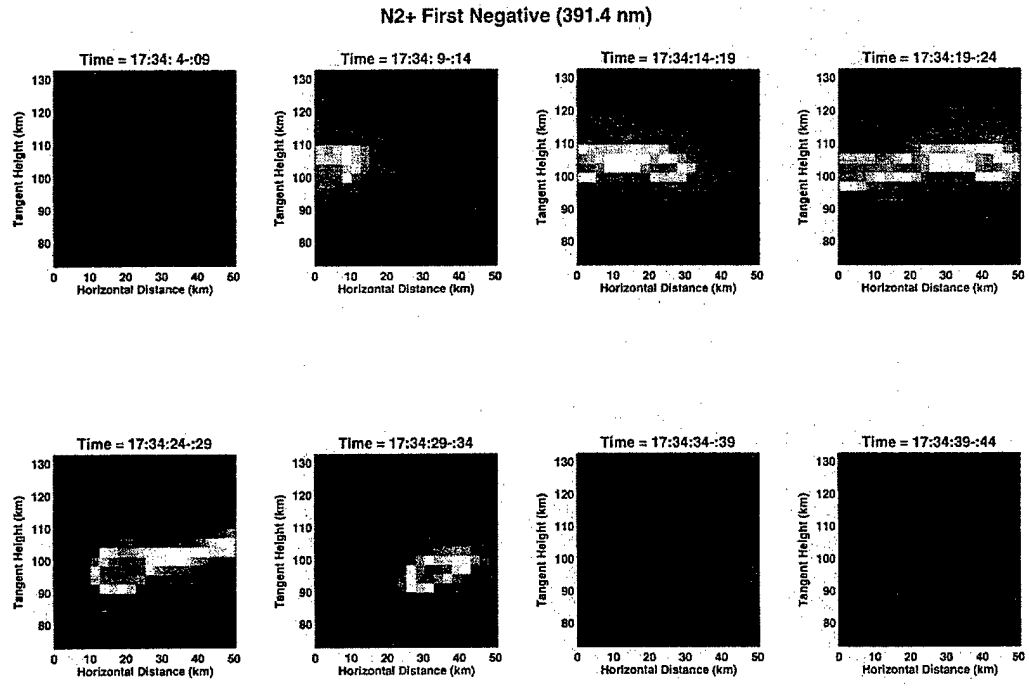

Figure 7. SPIM images of the 391.4 nm emission from N_2^+ during EL15050000301, as the MSX field of view drifts through a region with a high level of auroral dosing.

The excellent temporal and spatial resolution of the SPIM data are evident in Figures 7-9, which zoom in on the moments of this DCE when the instruments recorded the greatest auroral activity. Figure 7 shows eight SPIM images in the 391.4 nm sub-band. Each was acquired during a 5-second interval during which the mirror scanned its full range from top to bottom, or vice versa, so the sequence comprises 40 seconds worth of data. In the first image, the edge of the auroral dosing region is beginning to drift into view. In subsequent images, it begins to overspread the field of view, and eventually (in the fourth image) three bright distinct spots are visible. After the third bright spot drifts out of view, the emission appears to come from lower and lower tangent heights, as is also shown in the overview in Figure 4a.

Image sequences using the 557.7 and 337.1 nm sub-bands look very much like this, as well. Even for the O_2 Atmospheric band at 762 nm, the pattern is quite similar, as can be

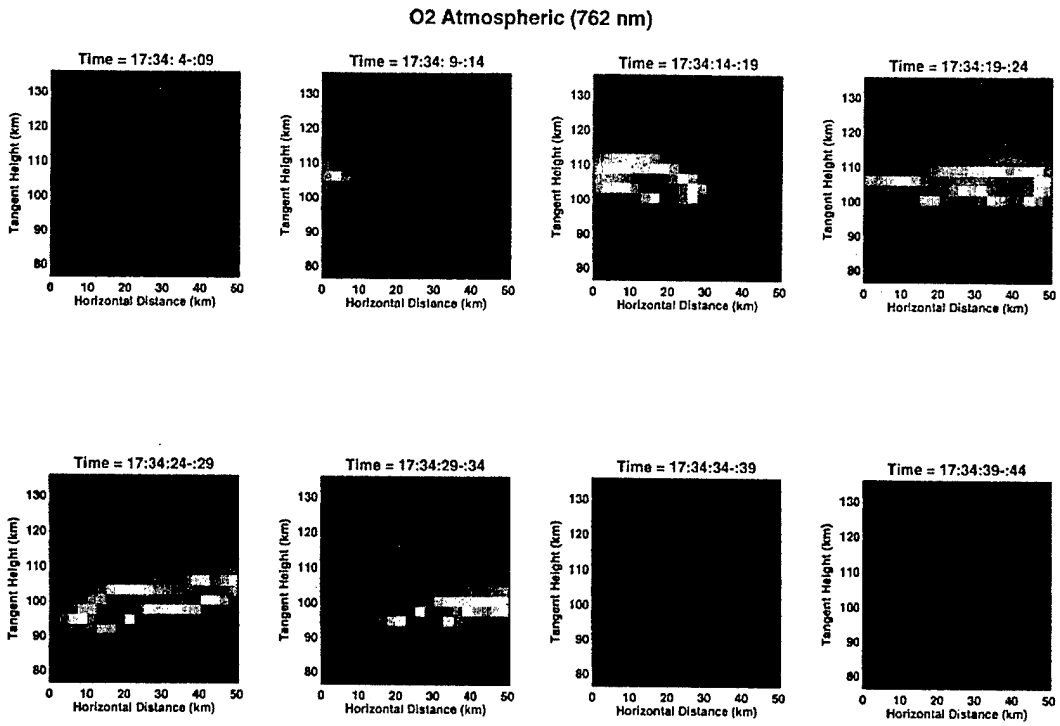

Figure 8. As Figure 7, but for the O_2 Atmospheric band emission at 762 nm.

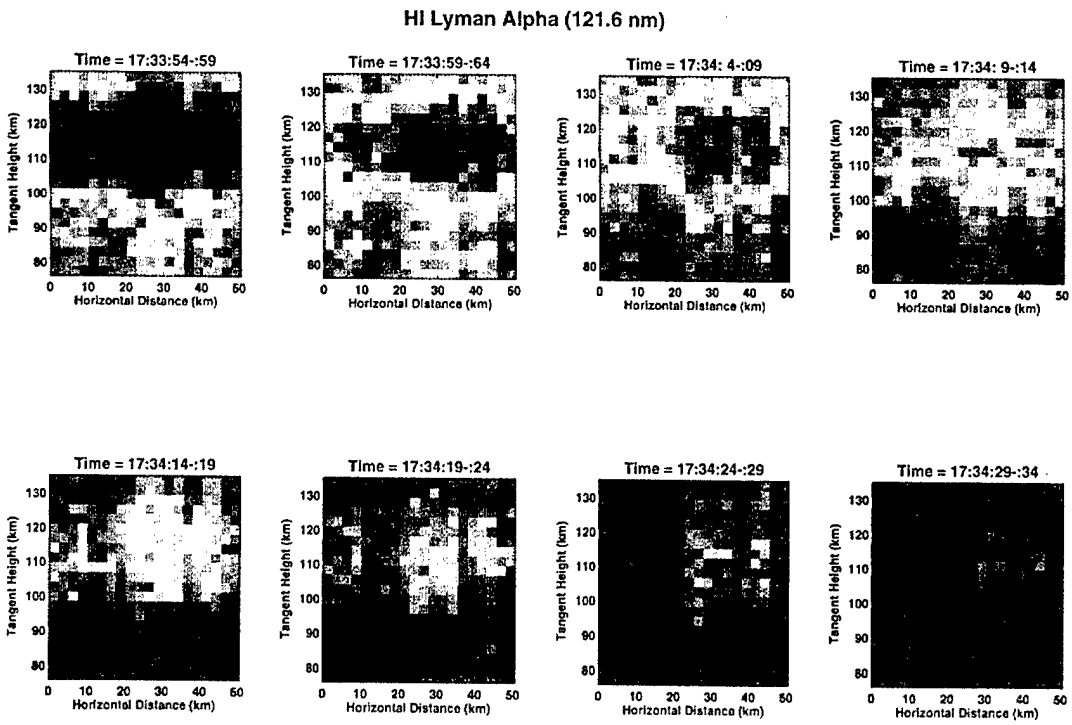

Figure 9. As Figure 7, but for the HI Lyman α emission at 121.6 nm.

seen in Figure 8. In terms of photon count, that band is the brightest emission seen by the SPIMs, with peak radiances of 2.5 MR.

As one might expect, the Lyman α images are quite different. The sequence shown in Figure 9, having a much more diffuse emission pattern, starts ten seconds before the other sequences. But it records the time that the proton aurora (as seen by MSX) was dying out, so the intensity diminishes uniformly in these frames even though the view is of the region where electron precipitation was building up.

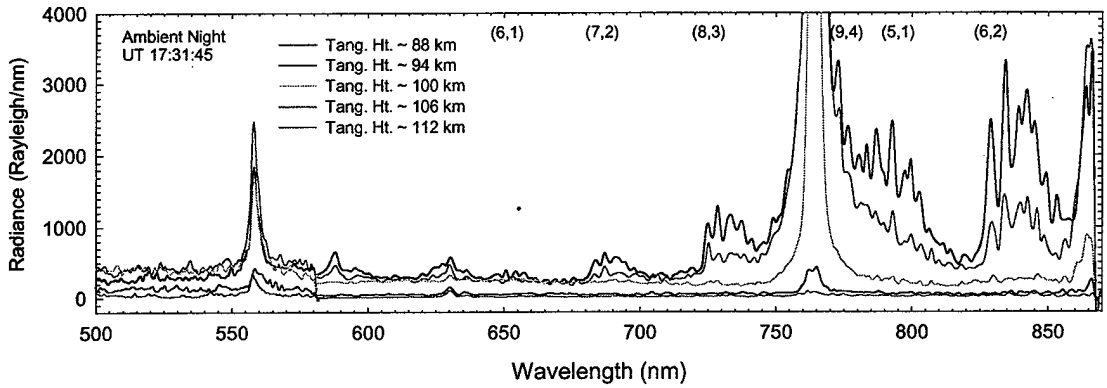

Figure 10. SPIM spectra from EL15050000301, for quiescent nighttime conditions.

The rich spectral content that is evident in Figures 2 and 3, and the spatial variability that is most clearly seen in Figures 7 and 8, are primarily due to the aurora. At the beginning of this DCE, however, quiet conditions prevailed near the tangent point. Spectra taken during the first two minutes therefore contain very weak (or, by comparison, nonexistent) emissions at the higher altitudes and shorter wavelengths. Figure 10 displays spectra from SPIMs 3-5 corresponding to some of the lower limb views. Aside from the green line at 557.7 nm and the O_2 Atmospheric bands, the primary features are the OH Meinel bands ($\Delta v=4$ and $\Delta v=5$) in the visible and NIR. In particular, the (6,2) and (5,1) bands stand out near 840 and 790 nm, respectively, as do the (8,3) and (7,2) bands near 735 and 690 nm. However, many OH lines in other bands that are weaker or partially obscured by competing emissions can also be identified. One can see that, unlike the auroral data, there is virtually no signal above 112 km throughout most of the spectral range, although atomic oxygen emissions that probably originate above the tangent point can be discerned.

As a footnote to this discussion, it should be pointed out that the SPIM data that are described here have been used to supplement data from other MSX instruments and, in so doing, to support several different scientific studies of the aurora. One study to which we contributed [*Sharma et al, 2001*] identifies the signature of the aurora in the emissions from nascent nitric oxide that were detected in the MSX Radiometer Band A (6.77-10.4 μm). The band A filter does not pass the 5.3 μm emissions from the fundamental $\Delta v=1$ band but it does pass longer-wave emissions from the hot bands, which are not produced in the quiescent atmosphere. Modeling showed that most of the chemiluminescent emis-

sion comes from the reaction of $N(^2D)$ with O_2. SPIM data, e.g. the 391.4 nm and LBH emissions, were required to determine the auroral dosing levels. To get quantitative results from the model, SPIM images (including the image sequences of Figure 7) were used to determine the strength of the dosing at precise locations within the horizontal field of view of the radiometer, which was repeatedly scanned back and forth through the dosing region. The results demonstrate the utility of obtaining multispectral data with high spatial and temporal resolution, a unique capability of MSX.

2.2 Observation of Stratospheric Waves

One of the very important results of the MSX mission was to demonstrate that MWIR radiance structure caused by atmospheric gravity waves (GWs) in the upper stratosphere can be measured by satellite-borne instruments. The optical signature of upward-propagating waves is typically seen in emissions originating in the upper mesosphere, so this discovery holds great hope for eventually studying GWs over a much broader range of altitudes than has been possible in the past, and hence learning much about the ways they evolve and propagate.

Dewan et al [*1998*] reported circular patterns in SPIRIT III Band B (CO_2 4.3 μm) data that were taken during two separate BTH Earthlimb experiments. Attributing these patterns to temperature perturbations in the upper stratosphere, they ultimately traced them back to locations where strong convective sources (thunderstorms) had existed an hour or so previously. Their argument that the thunderstorms were the sources of the observed ringlike radiance structure is boosted by calculations based on gravity wave theory, and also by calculations of the emission of the 4.3 μm radiance and its propagation to satellite altitudes.

Our role in this work involved the CO_2 radiative transfer calculations, and is reported by Picard et al [*1998*]. That paper, which constitutes Appendix A of this report, describes both the phenomenology that was observed and the calculations supporting the interpretations that were made. A very brief summary of the latter is given below.

The radiance structure observed by MSX [*Dewan et al, 1998; Picard et al, 1998*] comprises a rather small perturbation atop the observed radiance—only 1.5 to 2 percent of the total. The interpretation of this structure as a thunderstorm-induced wave, or at least the determination of the wave parameters, relies upon knowing the altitude at which it originated. This is because the observed horizontal wavelengths, the distances to the purported source points, and the propagation times constrain the altitudes at which temperature/pressure variations can be present [*Dewan et al, 1998*].

The altitude range for these emissions was established by calculating contribution functions (CFs) for the Band B bandpass. The CFs basically break out the different contributions to the total observed LOS radiance according to the layers of the atmosphere within which they originate. That is, the number of photons arising in a given layer and surviving the transit to the detector constitute the contribution from that layer, and the sum of all such quantities over the path gives the total observed radiance. CFs depend on the path through the atmosphere (e.g., the nadir angle), the temperature structure, the solar zenith angle and a number of other things. As shown by Picard et al [*1998*], for conditions appropriate for the MSX observations they peak at about 40 km, with a HWHM of about 10 km. It was thus inferred that the radiance structure arises in the upper stratosphere,

which is consistent with the constraints imposed by the observations and the gravity wave theory.

CFs were calculated using FASE, a line-by-line radiance code that fully accounts for the strong overlap of spectral lines that occurs in the 4.3 μm region. These results not only establish the principal source region for the observed radiance, stated above, but also rule out periodic cloud structure as an alternative explanation because tropospheric contributions would be much too small. (It is true that Band B actually had two filters; one was sensitive to low-altitude emissions, but the other was not. See the paper by Picard et al in the appendix.) The CF calculations incorporate non-LTE effects, because the CO_2 states are strongly pumped by absorption of solar flux in the mesosphere. Using the ARC code, we calculated the vibrational temperatures of these states for a solar zenith angle of 73°, for use by FASE. The non-LTE contributions to the observed radiance are not negligible despite the reduced density of emitters at high altitudes, but they are small enough that the essential conclusion about the altitude of the source region is unaffected.

In addition to the conclusions that have been summarized above, this work has led to an ongoing effort to model GWs and resulting MWIR radiance structure. Among the objectives are quantifying the structure amplitude for different conditions, and determining if and when high-altitude non-LTE effects might obscure or partially obscure the signature of the stratospheric perturbations. Another objective is to learn more about the effect of the viewing geometry, e.g. the direction of propagation of the phase fronts with respect to the LOS, on the detectability of the waves. (For a LOS crossing many peaks and troughs of the wave, the structure will average out and not be seen.) A final objective is to help determine an optimal configuration (including passbands and viewing conditions) for a proposed satellite wave detector.

3. ARC Transfer Functions

3.1 Introduction

Atmospheric Radiance Code (ARC) is the AFRL non-LTE research code (or, more accurately, the set of codes) used for investigating problems involving atmospheric infrared emissions from CO_2 and other molecules, and the processes that produce these emissions. We have been responsible for writing and maintaining the code, and upgrading the underlying model. We have made a number of changes to improve the non-LTE calculations in ARC. Some of these were designed to make it possible to apply the component codes to problems involving atmospheric structure; others address the not-unrelated problem of making it run a lot faster than it originally did.

The principal advance that has been made is the full implementation of the ARC transfer functions in RAD and RADC. These are the codes that calculate vibrational temperatures of various infrared CO_2 and CO states that are significantly influenced by radiative transfer within the atmosphere. The direct purpose of the transfer functions is to bypass the most computation-intensive calculations, the line-by-line (LBL) integration of radiative absorption at all altitudes. This speeds up the iterative process that determines the radiative excitation of the infrared-active states, and hence the vibrational temperatures.

The basic procedure in RAD and RADC was, and remains, to (1) assume some initial condition for the populations of all the emitting states at all altitudes; (2) use these to calculate the radiative absorption everywhere; (3) calculate new populations; and (4) iterate the process until convergence is achieved. The initial populations are generally, but not necessarily, taken to be LTE populations. The process is a simple lambda iteration.

In its original formulation [*Wintersteiner et al, 1992*], the algorithm always performed the full LBL calculation for all bands several times. During an initial LBL "regular iteration", the code would save all the layer contributions (defined below) for each altitude. It would next perform many fast "accelerated iterations" by substituting the new source function for the original first-guess source function in all the layer contributions. This sequence of one regular and many accelerated iterations would then be repeated, normally several times, to get the final result.

In the new formulation [*Wintersteiner et al, 1999b*], the stored quantities are the transfer functions rather than the layer contributions. The transfer functions still have to be calculated at some point for each band with the computation-intensive LBL integration algorithm, but there is no longer a need to repeat these "regular" iterations. Also, we now save and reuse the transfer functions for certain problems, completely eliminating the LBL integration for the majority of runs. As a result of all this, for runs when the transfer functions are calculated, convergence is faster and is achieved with a single LBL iteration. When pre-calculated transfer functions are used, the results are obtained with negligible computer time.

If the problem to which they are applied involves the same model atmosphere as that used to calculate them, the result is exactly what it would be if the full calculation were performed. With a single set of transfer functions, therefore, one can perform calculations for different solar zenith angles (or for day and night conditions), using different chemical or collision excitation processes or different rate constants to describe them, or differ-

ent densities for the collision partners. In all of these cases, the transfer functions preserve all the information from the full LBL calculation, and the results are exact.

One can also do calculations using a different thermal profile, or a different radiator density profile. In that case the results will be close to what one would get with a full LBL calculation (provided the profiles in the original run were not completely different) but they will not be exactly right. We show some examples of these results, below.

By "negligible" computer time, above, we mean that the calculation for many bands can be done in a second or two on a modern PC using stored transfer functions. This compares to 10 seconds or less for a single band for the LBL calculation, depending on the optical thickness, or about a minute for many bands. It is much less time than the original algorithm requires, and vastly less than the hours needed on the slower machines we used to develop it.

3.2 Formulation

The steady-state equations for n unknown vibrational populations can be written as

$$\frac{dN_l'}{dt} = 0 = \left\{ J_l N_l'' + \sum_{\substack{m=1 \\ m \neq l}}^{n} k_{lm}' N_l'' N_m' + C_l' + S_l \right\} - N_l' \left\{ A_l + \sum_{\substack{m=1 \\ m \neq l}}^{n} k_{lm} N_m'' + C_l \right\} \quad l = 1, \ldots, n \qquad (1)$$

where N_l' = unknown population of upper vibrational states, $l = 1, \ldots, n$

N_l'' = known population of lower vibrational states, $l = 1, \ldots, n$

J_l = radiative excitation from N_l'' to N_l'

A_l = Einstein coefficient for N_l'

k_{lm}, k_{lm}' = rate constants for collision process $l \leftrightarrow m$, $m = 1, \ldots, n$

C_l, C_l' = total rates for collision processes with known states

S_l = other excitation rates (solar, photochemical,...)

These equations quantify the balance between the rate of production of the lth unknown state (in the first set of curly brackets) and the loss (the following term). They are satisfied at the boundaries, z_i, of the layers in the atmosphere. Being linear in the unknowns, their solution is obtained simultaneously for all n states by matrix inversion. The solution for the different altitude levels is obtained sequentially, however, which is what makes the iteration necessary. Note that collisions are what couple the unknown states; we assume that there are no radiative transitions between them. Also, note that the notation (e.g., J_l) implies that there is only one radiative transition connecting each unknown state with a lower state. This is not necessarily so, but generalizing the equations to accommodate the alternative is straightforward.

All quantities in Eq.(1) are evaluated at the atmospheric grid points, z_i. Except for the radiative excitation, all the processes represented in the equation are local ones.

The expression for J_l was derived by Wintersteiner et al [*1992*], and the result is recast here in terms of transfer functions. J_l is expressed as a sum of contributions (layer contributions) from all the layers in the atmosphere. The layers are labeled by the index k, so

the layer contributions are the number of photons/(sec-cm^3) coming from layer k that are absorbed at altitude z_i. Quantities characteristic of a layer as a whole are evaluated at some mean position within the layer (as opposed to the layer boundaries) that we call $\overline{z}_k$. The "layer" denoted by $k=0$ is actually the lower boundary of the atmosphere, which is regarded as a blackbody surface. k_{max} is the number of ordinary layers. The radiative excitation is

$$J_l(z_i)N_l''(z_i) = \sum_{k=0}^{k_{\max}} W_{ik}^{(l)} = \sum_{k=0}^{k_{\max}} \alpha_{ik}^{(l)} T_{ik}^{(l)}, \tag{2}$$

where $W_{ik}^{(l)}$ = contribution of layer k to the absorption at altitude z_i,

$\alpha_{ik}^{(l)}$ = band-dependent coefficients that can be quickly updated, and

$T_{ik}^{(l)}$ = transfer functions containing all line-dependent quantities.

The superscript *(l)* identifies the band connecting to the lth state; in general, one would have a sum over bands, but here it is superfluous. The coefficients are given by

$$\alpha_{ik} = 4\pi\rho(z_i)\frac{Q_R''(T_s)}{Q_R''(T_i)}\frac{Q_V(T_s)}{Q_V(z_i)}\frac{\exp(-c_2E_V''/T_V''(z_i))}{\exp(-c_2E_V''/T_s)}\frac{\exp(-c_2E_V'/T_V'(\overline{z}_k))}{\exp(-c_2E_V''/T_V''(\overline{z}_k))}\frac{1-\Gamma(z_i)}{1-\Gamma(\overline{z}_k)} \tag{3}$$

where T_i = kinetic temperature at z_i,

T_s = HITRAN standard temperature, 296 K,

ρ = radiator density (mol/cm^3),

Q_R'' = rotational partition function of the lower vibrational state,

Q_V = vibrational partition function,

E_V', E_V'' = vibrational energy of upper and lower state (cm^{-1}),

T_V', T_V'' = vibrational temperature of upper and lower state, and

$\Gamma(z) = \dfrac{g_V''}{g_V'}\dfrac{N'(z)}{N''(z)}$, $\quad g_V', g_V''$ = vibrational statistical weights.

The lth band is implied. The double-primed quantities refer to the lower vibrational state of that band, while the single-primed quantities refer to the upper state. It is understood that $Q_V(T_s)$ is to be evaluated as an LTE quantity, while $Q_V(z_i)$ is evaluated using vibrational temperatures (populations) appropriate for altitude z_i. Note that in Eq.(3) all quantities have to do with the vibrational levels. The transfer functions are

$$T_{ik} = \frac{1-\Gamma(\overline{z}_k)}{1-\Gamma(z_i)}x \tag{4}$$

$$\sum_t \left\{ S(T_s)c\nu_t^2 \frac{\exp(-c_2E_R''/T_i)\exp(-c_2E_R'/T_k)}{\exp(-c_2E_R''/T_s)\exp(-c_2E_R''/T_k)}\frac{1-\gamma(z_i)}{1-\gamma(T_s)}\frac{1}{1-\gamma(\overline{z}_k)}\int_{-\infty}^{\infty} f_\nu(z_i)\Im_{\nu k}(z_i)d\nu \right\}$$

where the summation is over all ro-vibrational lines, t, in the lth band, the integration is over the tth line, and quantities in the sum are understood to characterize these transitions

(e.g., S) or the rotational states involved (e.g., E_R) rather than any vibrational state properties. The quantities in Eq.(4) are

E'_R, E''_R = rotational energy of the upper, lower states (cm^{-1})

$S(T_s)$ = HITRAN line strength at the standard temperature

c, c_2 = speed of light, 2nd radiation constant

ν_t = transition energy (cm^{-1}),

f_ν = normalized Voigt profile,

$$\Im_{\nu k}(z_i) = \begin{cases} E_2(\overline{\tau}_\nu[z_i, z_1]) & k = 0 \\ E_2(\overline{\tau}_\nu[z_i, z_{k+1}]) - E_2(\overline{\tau}_\nu[z_i, z_k]) & k = 1, \ldots, k_1 - 1 \\ E_2(\overline{\tau}_\nu[z_k, z_i]) - E_2(\overline{\tau}_\nu[z_{k+1}, z_i]) & k = k_1, \ldots, k_{\max} \end{cases}$$

E_2 = exponential integral of order 2

$\overline{\tau}_\nu(z, z')$ = optical depth between two altitudes at wavenumber ν

k_1 = index of the layer whose lower boundary is z_i

$$\gamma(z) = \frac{g''_R g''_V}{g'_R g'_V} \frac{n'(z)}{n''(z)} \quad \begin{cases} g''_R, g'_R = \text{rotational statistical weights} \\ n'', n' = \text{ro-vibrational state populations} \end{cases}$$

The source function, which in general is given for line t by

$$R(z) = 2c\nu_t^2 \frac{\gamma(z)}{1 - \gamma(z)}, \tag{5}$$

does not explicitly appear in the expressions above. This is because these expressions derive from the expansion of the source function $R(\overline{z}_k)$ and the line strength $S(z_i)$ into their component parts, which allows for the partition between vibrational and rotational quantities. This partition allows us to avoid repeating the LBL integrations because there is nothing within the ν-integral that changes during the iterative process. That is, vibrational populations do converge from the initial-guess values to the correct solution, but nothing about the rotational distribution or the optical path through the atmosphere is affected since the kinetic (rotational) temperature and the lower-state densities that are needed to calculate $\overline{\tau}_\nu$ are unchanged. Therefore, all that is required is to update the coefficients, α_{ik}, on each iteration by replacing the original upper-state vibrational populations with new ones, and then recalculate the sum, Eq.(2).

The particular form chosen for the coefficients, that is the inclusion of the radiator density and the lower-state vibrational properties that do not change from iteration to iteration, reflects our intention to extend the use of transfer functions to achieve rapid approximate solutions. Exact solutions can be obtained only when the kinetic temperature and lower-state number densities are unchanged from the original calculation, but small or modest changes in either of these can, in some circumstances, produce rather little change in T_{ik}. [The radiative absorption rate, $J_i(z_i)$, may more directly reflect changes in $\rho(z_i)$, for example, than changes in either of these, especially for thin bands.] Therefore,

it is useful to define the coefficients, α_{ik}, using quantities that may be different from the original calculation to the current one, which is why Eq.(3) is written as it is.

To be a little more specific, so long as the original model atmosphere is used in any transfer-function calculation, all factors involving lower-state distributions are constant and could be put into either the coefficients or the transfer functions. To extend the applicability, however, we have put as many terms as possible into the coefficients, leaving within T_{ik} only those that cannot be corrected without repeating the LBL calculation. The most important remaining quantities are the rotational population distributions as given by the terms like $\exp(-c_2 E_R'' / T)$ (but for both the upper and lower ro-vibrational states), and the layer-to-point optical paths given by the $\overline{\tau}_v$. The effect of not being able to correct these quantities in a transfer-function calculation depends on how big a change has occurred in either T or the lower-state population densities. But any possible changes in other quantities can be accommodated by putting them into the α_{ik}.

One can speculate about whether the failure to correct the rotational distributions, or the layer-to-point optical paths, would have a greater effect in any given case. Since the total rotational population does not change even when the rotational distribution changes, one might think that because of the sum over lines the temperature would have the lesser effect on T_{ik}. However, in many bands most lines are thin over much of the altitude range under consideration, so in these cases an opposite conclusion might be warranted.

What was stated earlier about the separability of the vibrational and rotational quantities in α_{ik} and T_{ik} is actually true only to an excellent approximation. The $1-\gamma$ terms in (3.4) that represent stimulated-emission corrections to the line strength and the source function do in fact depend on the vibrational populations, because the rotational populations do. These terms are generally close to unity, however, and since they are accommodated in the original LBL calculations what is relevant is the change (as the iterations proceed) from their original value rather than the actual deviation from unity–that is, a small change in a small quantity. Their effect is noticeable only in the calculation for the CO_2 15 μm states, the lowest-energy infrared transitions we treat; it is utterly negligible for MWIR transitions.

To obtain the fastest possible convergence of the15 μm calculations, we treat stimulated-emission corrections in the transfer functions anyway. Note that the $1-\Gamma$ ratios in Equations (3) and (4) algebraically cancel each other perfectly, when the product is taken in Eq.(2). The values originally stored in the transfer functions in Eq.(4), however, are not exactly what is later calculated in Eq.(3) if the vibrational populations have changed, so the change in stimulated emission actually is included when the coefficients are calculated. The treatment is not exact since stimulated emission is different for each line, but the $1-\Gamma$ corrections are actually an excellent approximation to the average effect of the $1-\gamma$ terms that cannot be extracted from the sum in Eq.(4).

To summarize, one can say that the transfer functions express contributions of different regions of the atmosphere to the radiative excitation in a band in terms of invariant quantities, as nearly as that is possible. T_{ik} is actually proportional to the probability per unit time that a photon emitted in the kth layer is absorbed at z_i, and it has the same units

as Einstein coefficients, transitions/(mol-sec). Like the band-averaged Einstein coefficients in Eq.(1), it is weakly dependent on temperature and independent of most other elements of the atmospheric state vector.

The transfer functions can be used to give exact vibrational-temperature results extremely rapidly for many different cases. This means that one can do the LBL calculation once and then use the transfer functions to calculate the same states' populations using different assumptions about the kinetic processes, different solar excitation rates, etc. However, they cannot completely eliminate the effects of changing the temperature or the opacity of the atmosphere occurring when functions calculated for one scenario are applied to a different one.

3.3 Convergence

The convergence of the LBL calculation has been improved by the form chosen for the transfer functions. Figures 11a and 11b illustrate the convergence for the major-isotope CO_2 (01101) state, which involves radiative transfer in the ν_2 fundamental band. The calculation was carried to completion using two regular (LBL) iterations and a number of accelerated iterations. The vibrational temperatures at each step were recorded and later subtracted from the final values. The figures show these errors, for selected altitudes in the mesosphere and lower thermosphere, as they diminish from iteration to iteration.

In Figure 11a the stimulated-emission correction that was mentioned above was not included; in Figure 11b it was. Iteration #0 represents the initial condition. For both cases, iteration #1 was a LBL calculation, and was followed by 35 accelerated iterations, by a second LBL calculation, and then again by further accelerated iterations. In Figure 11a, the break at iteration #36, the second LBL iteration, reflects two things. The first is the fact that, as the upper-state 01101 populations evolve, the ground-state populations change very slightly (in a manner taken into account through the vibrational partition function) and as a consequence the optical paths between the source layers $(\overline{z}_k)$ and the absorption grid points (z_i) change as well. The latter change cannot be accounted for by the transfer functions, but it is accommodated when they are updated at iteration #36. The second thing is the stimulated emission correction to the line strength, which also changes slightly and affects the absorption rate. In Figure 11b, the latter is dealt with in an approximate manner, through the $1-\Gamma$ terms in Eqs. (3) and (4). That accounts for the differences between the two figures.

A number of conclusions can be drawn from these plots [*Wintersteiner et al, 1999a*]. The most important are that the convergence is rapid, and that the second LBL iteration is totally unnecessary (because of the high accuracy achieved without it). One should note that the initial assumption was that 01101 was in LTE at all altitudes, which means the first-guess temperatures were many degrees from the final (correct) results. Also, one can see that the stimulated-emission correction makes only a modest difference here.

Figures 12a and 12b give the same information, but for calculations using the first ν_2 hot band. The opacity in this band is less than in the fundamental, so convergence is achieved with many fewer iterations. Also, the lower-state population does not vary from iteration to iteration, so the break that occurs in 12a after the second LBL iteration is entirely due to the fact that the line strengths are affected slightly by stimulated emission.

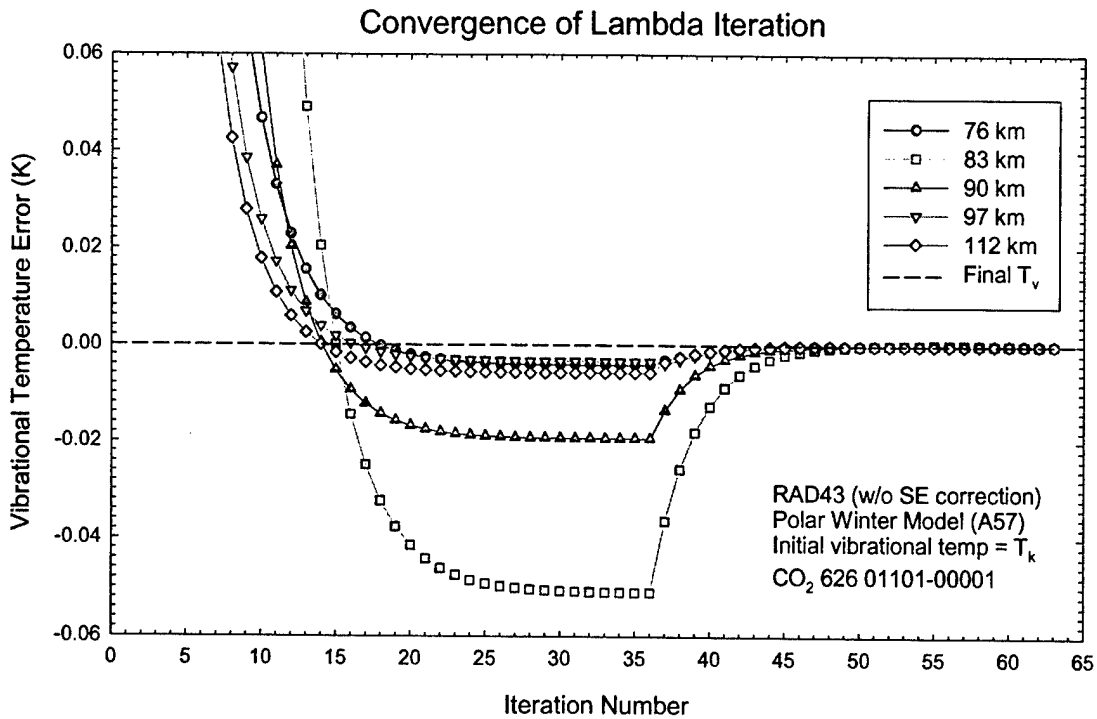

Figure 11a. Convergence of the lambda iteration, for the CO_2 626 ν_2 fundamental band during the process of calculating the 01101 populations. The stimulated-emission correction was not applied

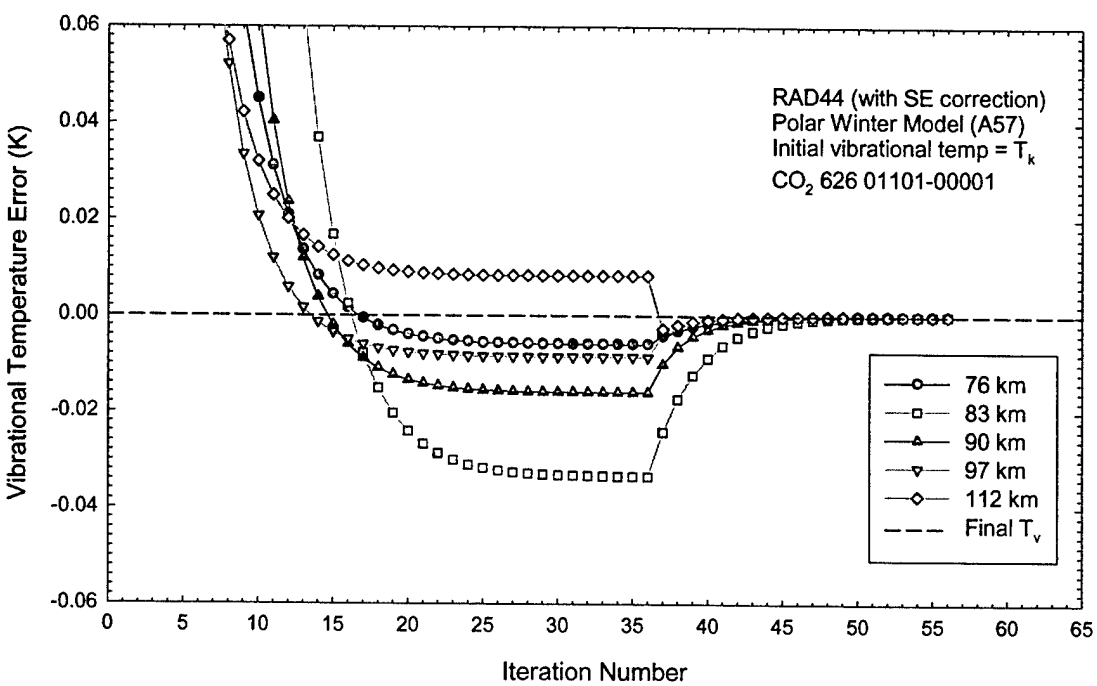

Figure 11b. As Figure 11a, but with the stimulated-emission correction applied.

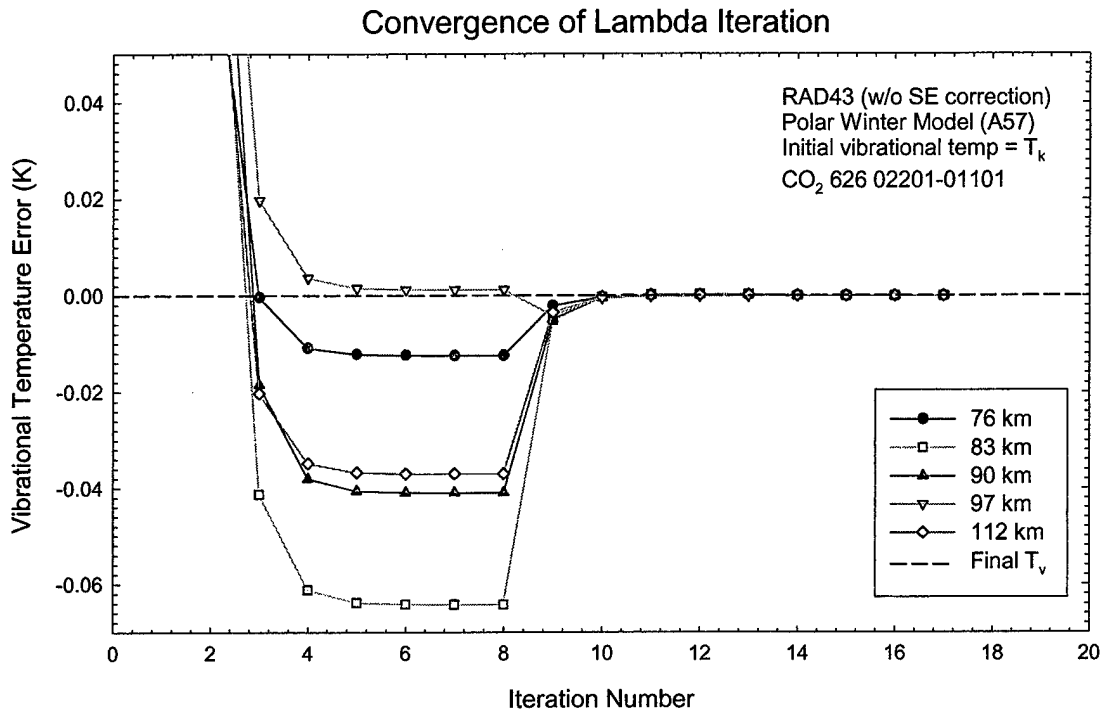

Figure 12a. Convergence of the lambda iteration, for the CO_2 626 first ν_2 hot band during the process of calculating the {10002-02201-10001} populations. The stimulated-emission correction was not applied.

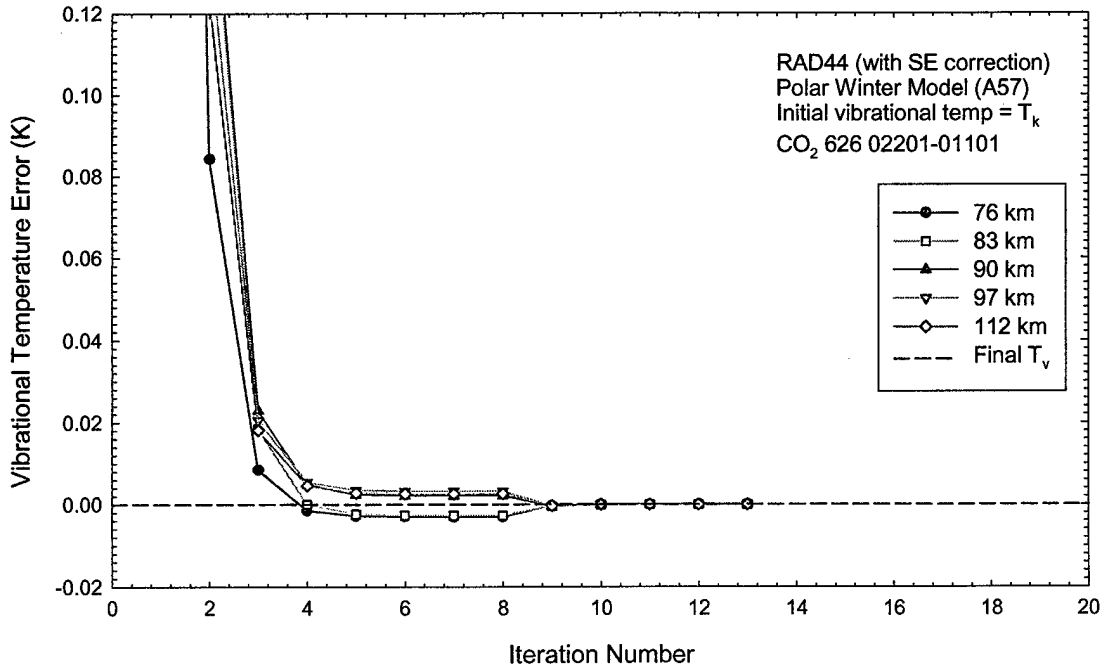

Figure 12b. As Figure 12a, except the stimulated-emission correction was applied.

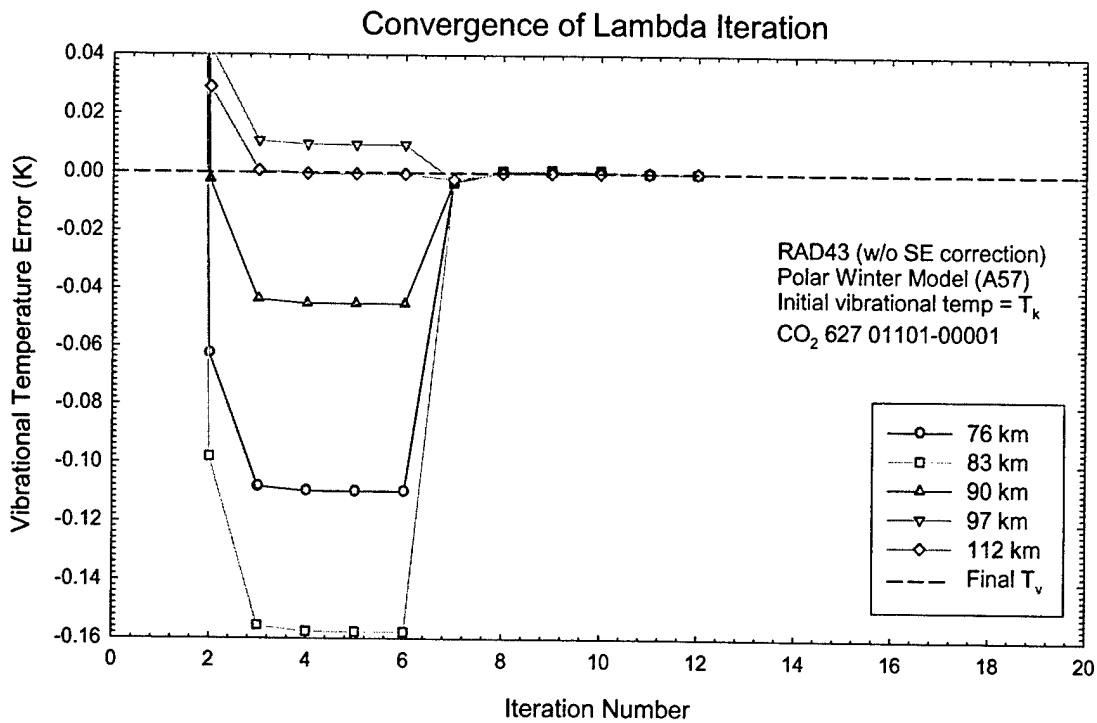

Figure 13a. Convergence of the lambda iteration, for the CO_2 627 fundamental band during the process of calculating 01101 populations. The stimulated-emission correction was not applied.

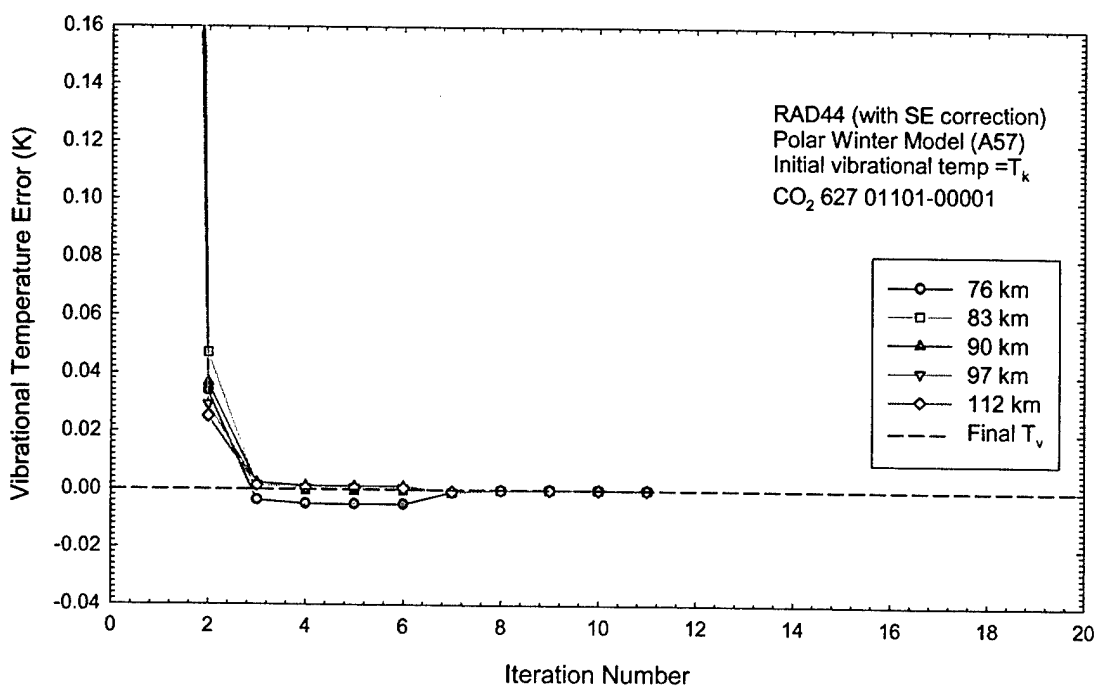

Figure 13b. As Figure 13a, except the stimulated-emission correction was applied.

In Figure 12b, that break is hardly seen because the approximate stimulated-emission correction is effective in removing it.

Figures 13a and 13b show the convergence of the calculation for the 627 01101 state. The 627 fundamental band is optically much thinner in the mesosphere than the 626 band is. The result is that many fewer iterations are needed and the errors, such as they are, that remain after the first set of accelerated iterations are again due to the inability to correct for stimulated emission. In this case the layer-to-point optical paths also change from iteration to iteration as they did for the major-isotope calculation (Figure 11), but this is basically irrelevant since most of the lines are thin in the altitude range where that occurs.

The model atmosphere used in the calculations shown in Figures 11-13 was a climatological polar winter model, which has a cold stratopause and a warm mesopause. Convergence of calculations using polar summer and midlatitude models is equally rapid, even though in that case the initial-guess profiles (again set equal to the kinetic temperature) were farther from the final solution over much of the range in both cases. The accuracy for the ν_2 states that is achieved with a single LBL iteration is generally comparable to what is shown in Figures 11b-13b, but even in the worst case is better than 60 mK when the stimulated-emission correction is applied.

We did further tests by initializing the vibrational temperatures with very unrealistic profiles (for example, 250 K at all altitudes). The number of iterations required was generally greater for those tests, but in the end the solutions were identical to those attained when the initial condition was the kinetic temperature.

The 4.3 μm CO_2 bands are much thicker than the 15 μm bands. As a result, convergence generally requires many more accelerated iterations for the asymmetric stretch states than for the bend-stretch states. However, stimulated emission is a completely negligible correction for these bands, so a second LBL iteration does not improve the convergence at all, even on the scale (tens of mK) of Figures 11-13.

3.4 Application of Stored Transfer Functions

As stated earlier, the new transfer-function formalism provides the capability for modeling many scenarios with the same stored transfer functions. We have utilized this capability for repeated calculations many times. A simple example is given in Figure 14, where we plot vibrational temperatures of some of the bend-stretch states. The strongly coupled {10002-02201-10001} states are excited primarily by VT processes due to the major atmospheric constituents and by radiative excitation from within the atmosphere. There is also some production (and loss) resulting from collisions that exchange quanta with the 00011 state, and due to VV exchange with N_2 that couples them to the so-called Group 1 states {10012-02211-10011}. The latter mechanisms are not important at night, but they do make a difference in the daytime when the higher-lying states are pumped by solar flux. The first of these also affects the {11102-03301-11101} states.

The calculation in Figure 14 demonstrates the effect of these processes. It was done for a midlatitude model atmosphere similar to the U.S. Standard Atmosphere. The kinetic temperature profile is plotted on the left-hand side, together with the vibrational temperatures for nighttime and for daytime using a solar zenith angle (SZA) of 60 degrees. The day-night differences using two solar zenith angles, 60° and 80°, are given on the right.

All calculations were performed with the same transfer functions. Since the only difference between the daytime and nighttime calculations was the rate of excitation of the bend-stretch states by collision processes, the results are exactly what they would be if all the calculations had been done independently with LBL calculations. Similarly, if the daytime atomic oxygen profile had been assumed to be different from that at night, the results would still be exactly correct. However, if the kinetic temperature structure had been assumed to be different, some error would have been inevitable.

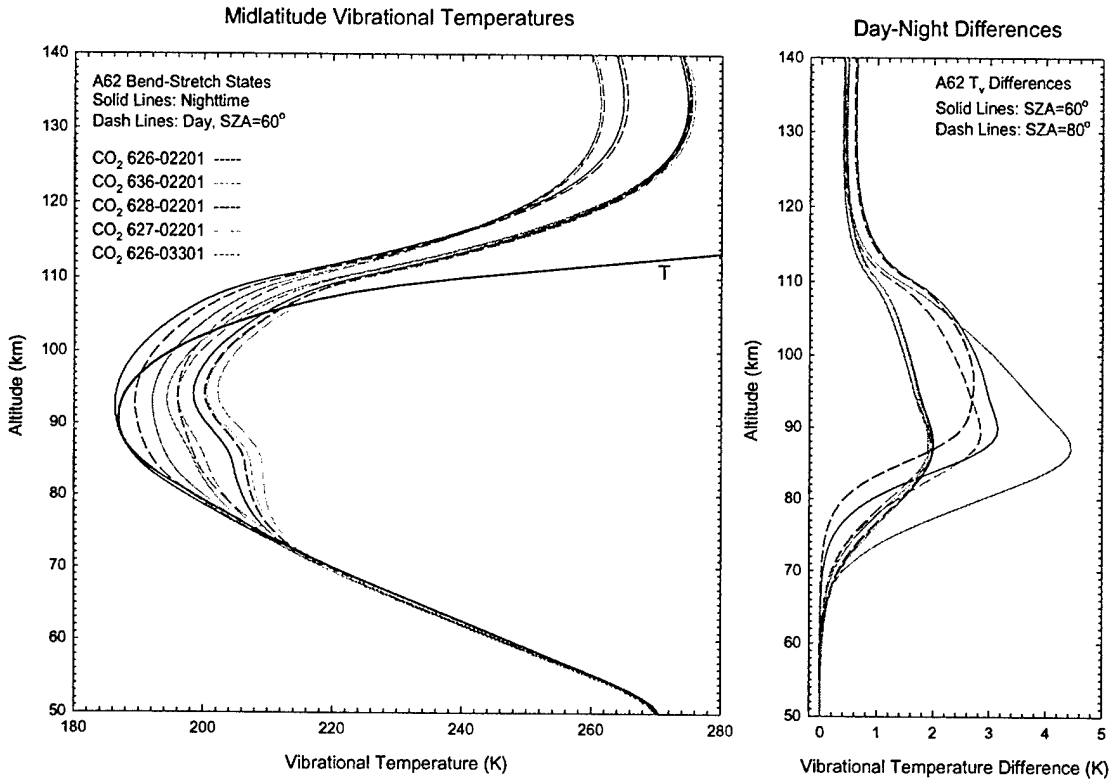

Figure 14. Vibrational temperatures for some CO_2 bend-stretch states that are affected by solar pumping. The day-night differences for these states are plotted on the right.

The 00011 vibrational temperatures, day and night, that were needed for that calculation were also generated using a single set of transfer functions for the ν_3 bands.

We have done many calculations that apply transfer functions generated from one model atmosphere to other models with different temperature and pressure profiles. One purpose for doing this is to assess the applicability of the process to situations with variable atmospheric structure, in which a potentially large set of perturbations to nominal background conditions must be considered. Another was to test the feasibility of using the model as a component of a non-LTE temperature retrieval algorithm, in which the temperature/pressure profile would evolve from some assumed initial state to a final con-

verged one. While performing the latter exercises as part of the SABER operational software development process, we did the calculations shown in Figures 15 and 16.

In each case shown in these figures, we took a climatological model atmosphere and computed the transfer functions for the bend-stretch (15 μm) states. For Figure 15, we used the midlatitude model similar to the U.S. Standard Atmosphere, whose temperature profile is given in Figure 14. Then we made an *ad-hoc* adjustment to the atmospheric state vector. This consisted of (1) increasing the temperature from the original profile by exactly 10 K at all altitudes above 60 km, and increasing it by 0 to 10 K in the 50- to 60-km region; and (2) adjusting the pressure to satisfy conditions of hydrostatic equilibrium. The test consisted of calculating the vibrational temperatures for the new "perturbed" atmospheres using the original transfer functions, and once again using the full LBL calculation, and comparing the results. The full calculation of course gives the correct results, but the fast transfer-function calculation gives quite a good approximation. The left-hand part of Figure 15 shows the vibrational temperatures of six bend-stretch states, calculated both ways, for the 60 to 120-km altitude region that is most significant for the retrieval problem. Since the curves are barely distinguishable, the differences are given on the right. One can see that the approximate results have a worst error of ~1 K, which is only 10% of the perturbation of the kinetic temperature profile that we imposed. Most of the states are calculated to within 0.4 K, or 4% of the perturbation.

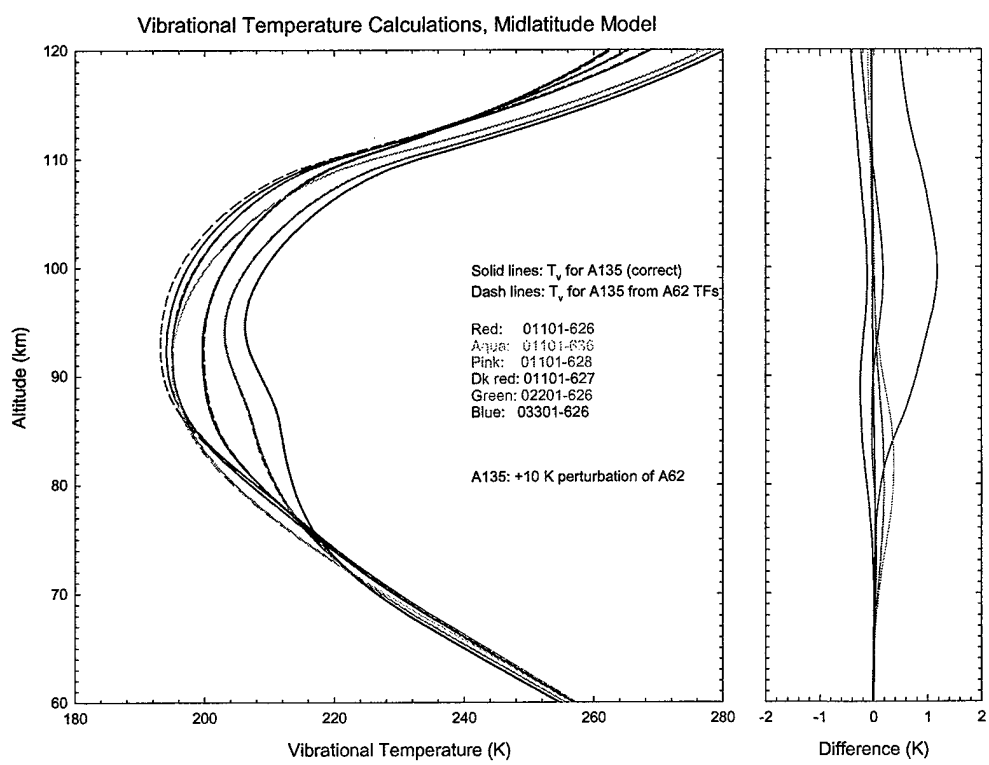

Figure 15. Comparison of LBL and transfer-function calculations. The midlatitude model whose temperature profile is given in Figure 14 was used to generate the transfer functions. The vibrational temperatures are for a calculation using a modification of this profile, as described in the text. In the left-hand plot, the solid lines are the LBL calculation and the dashed lines give the approximate results.

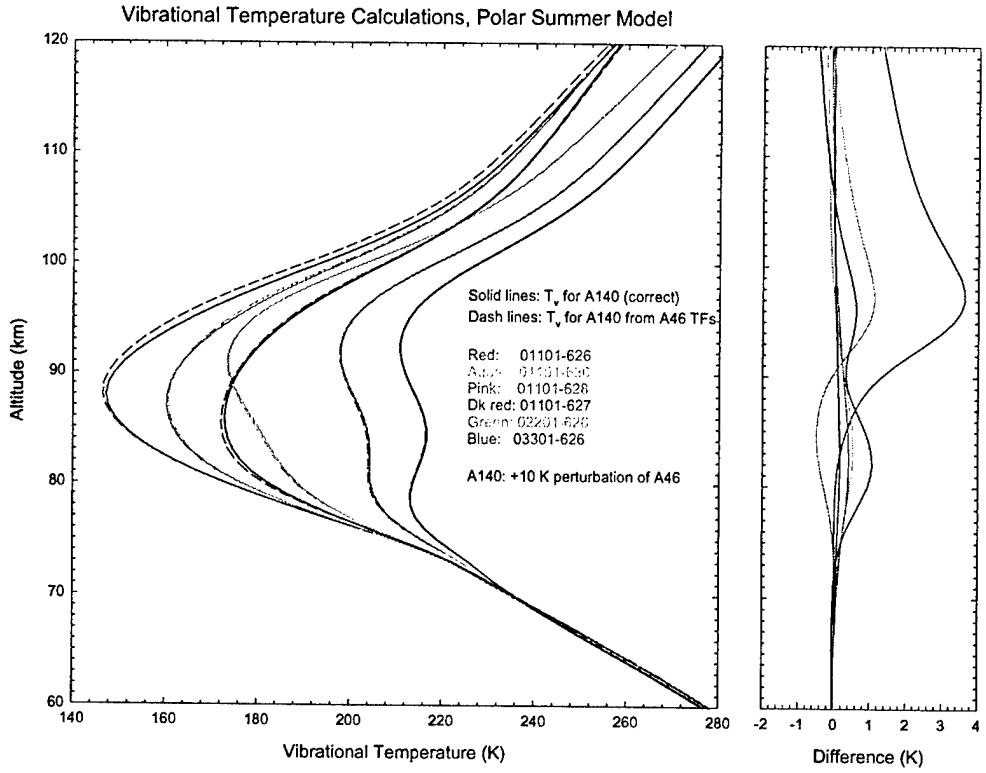

Figure 16. As Figure 15, except that the original model atmosphere was a polar summer model (not shown) The perturbed model for which the calculations were performed was derived from it by the same procedure, described in the text, as that used for the profile in Figure 15.

Figure 16 shows the same sort of calculation using a polar summer model atmosphere. In this case the mesopause temperature was below 140 K and the temperature gradients were much steeper, making it a more stressing case. The state with the optically thickest band was in error near the mesopause by as much as 3 K, while the thinner bands once again were calculated more accurately. Among a number of tests we made, involving different model atmospheres and different perturbations, this was the worst result.

It should be emphasized that this particular sort of test, in which the temperature is increased (or decreased) uniformly from the original profile, presents more of a challenge to the approximate algorithm than most others, because there is little opportunity for errors of different sign to cancel each other. Tests in which the temperature perturbations oscillate about the assumed background state are different in this respect; however the period, amplitude, and symmetry of the perturbations would surely influence how closely the correct results can be approached.

In Figure 17 we show a very structured model atmosphere, and vibrational temperature results presented as in Figures 15 and 16. In this case we used an experimental temperature profile, obtained by Rayleigh lidar during the ALOHA '93 campaign [*Dao et al, 1995*], to test the algorithm for a case with wavelike structure. We averaged the temperature data into 0.2 km bins, and wrote the profile onto a variable grid that preserved all

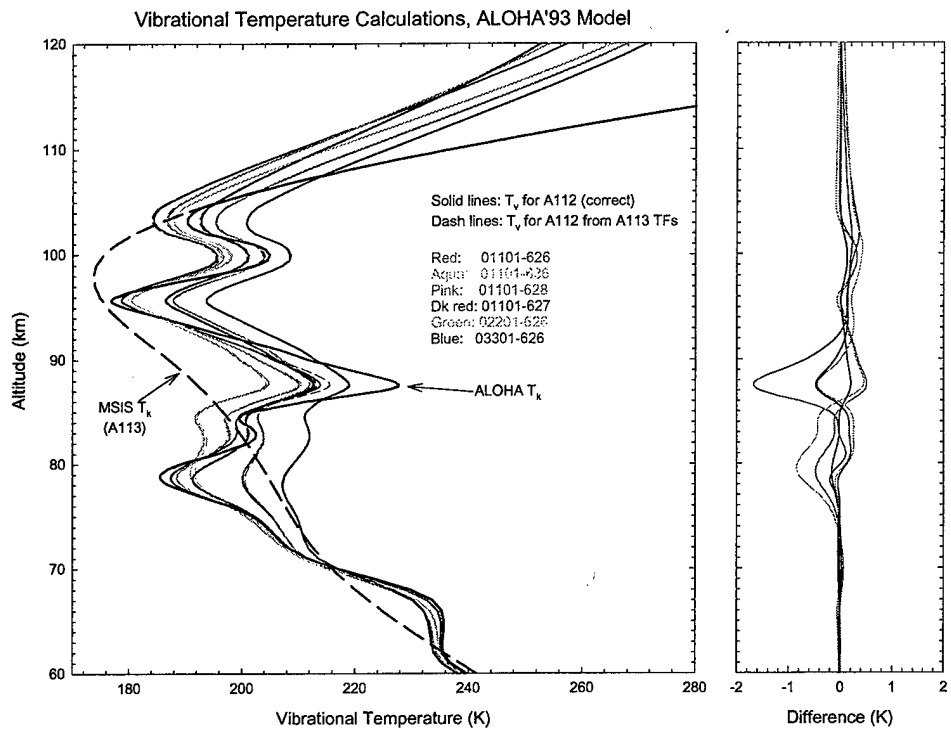

Figure 17. Comparison of bend-stretch vibrational temperatures from a full LBL calculation (solid lines) and from a transfer function calculation (dashed lines). The climatological temperature profile used to generate the transfer functions is labeled MSIS; the structured profile for which the comparison is made is labeled ALOHA. The vibrational-temperature differences are shown on the right.

structure remaining at that resolution, so the grid was degraded to 1 km over most of the altitude range but not at altitudes where extrema occur. We also ran MSIS-90 to get a climatological profile appropriate for the time and conditions when the measurements were taken. These two temperature profiles are plotted on the left hand side of Figure 17, and the lidar profile can reasonably be seen as a perturbation of the climatological temperature. (They are identical above 104 km, where lidar data were unavailable.) We took the density profiles from the MSIS run and, using the lidar temperatures, adjusted them for hydrostatic equilibrium to complete the wave-structured input model. Then we generated transfer functions using the smooth MSIS profile, applied them to the structured ALOHA atmosphere, and finally re-did the latter calculation using the full LBL procedure. We compare the results directly in the left-hand side of the figure, and plot the differences on the right.

Clearly the transfer functions provide an excellent approximation to the correct vibrational temperatures for the bend-stretch states in this example. Whereas the structured temperature profile differs from the climatological one by tens of degrees over much of the altitude range considered, by as much as 40 K at one point, no state is in error by as much as 2 K anywhere. In fact, no state is in error by even 1 K except for the major-isotope 01101 state in a very narrow range of altitudes. These calculations, and others we

have done, validate the transfer-function approach as a suitable means of calculating vibrational temperature profiles extremely quickly, for a variety of atmospheric conditions.

We have found that the transfer functions often, although not always, give better results for thinner bands when applied to models that are different from those from which they are generated. For example, in the difference parts of Figures 15-17, in each case the worst error occurs in the 626 01101 calculation, which involves radiative transfer in the thickest ν_2 band. As noted earlier, the main factors that cannot be corrected are the rotational distributions and the layer-to-point optical paths. This result suggests that for the 15 μm bands, the effect of opacity is greater.

As stated in the discussion following Eq. (1), the formulation given above has been implemented using an altitude grid. An alternative, perhaps more natural, approach would be to perform the calculations on a pressure grid. For the full LBL calculation it would not make any difference which is used. But for transfer-function calculations involving different temperature/pressure profiles, the optical path from a given layer to a given absorption grid point could be made approximately the same regardless of this if all the grid points were defined in pressure coordinates. This should minimize the effect of not being able to update the $\overline{\tau}_\nu$ residing within the transfer functions.

This is not necessarily true in a space defined by altitude alone. When one changes the temperature profile, one also changes the pressure in order to retain hydrostatic equilibrium throughout the atmosphere, so the point-to-point column densities automatically are altered. This is what was done for the calculations of Figures 15-17. It may be that the excellent results in Figure 17 come about partially because many of the changes in optical path for that case reflect increased and decreased density in different portions of the path, and so cancel to some extent. This does not happen with the calculations in Figures 15 and 16.

In an attempt to neutralize the effect of changing opacity, we simulated the process of performing calculations on a pressure grid. We did this for several of our test cases with modified atmospheres by using altitude grids that were carefully chosen so that the grid points occurred at exactly those altitudes having the same pressures as the grid points in the original calculation. A simulation was necessary to avoid rewriting the entire code in pressure coordinates.

The specific test was as follows, using the example of the perturbed midlatitude atmosphere that was described in conjunction with Figure 15. We had the transfer functions from the original midlatitude model, which were calculated for a 1-km grid between 40 and 160 km. We had perturbed the original model by changing the temperature by +10 K and established hydrostatic equilibrium for the new model. And we had done both the LBL and the transfer-function calculations on the original altitude grid as described earlier, with the resulting differences (errors) shown in the right-hand panel of Figure 15. Then we took the pressures corresponding to the original altitude grid, and looked at the perturbed model atmosphere to determine exactly what altitudes corresponded to those pressures. These altitudes, which were not exactly uniformly spaced, constituted a new altitude grid, and we mapped the modified atmospheric state vector onto this grid so we could redo the calculation with the LBL code. (These LBL results fell exactly on top of the LBL results done on the altitude grid, so they appear to be equivalent as they should

be. But with the different grids they could not be subtracted directly.) Finally we took the original transfer functions and used them on the modified grid, subtracting the results from the last LBL calculation to determine the errors.

Results are shown in Figure 18 for two such tests. One is the example we described, and the other is an "opposite" test case, using the same midlatitude model to start but with a negative temperature perturbation of 10 K rather than a positive one. This second test produced yet another altitude grid and another remapping of the atmospheric state vector. In the figure, we compare results only for the 626 01101 state, for these two test cases. "A62" refers to the original midlatitude model, whose kinetic temperature profile is again given in the left-hand panel. "A135" and "A136" refer to the models with kinetic temperature changed by +10 K and –10 K, respectively, and the LBL vibrational temperatures for the 01101 state for each of these are also given on the left for comparison. On the right are the errors, namely the differences between the LBL and the transfer-function results, as determined using the original procedure ("altitude grid") and the simulation ("pressure grid").

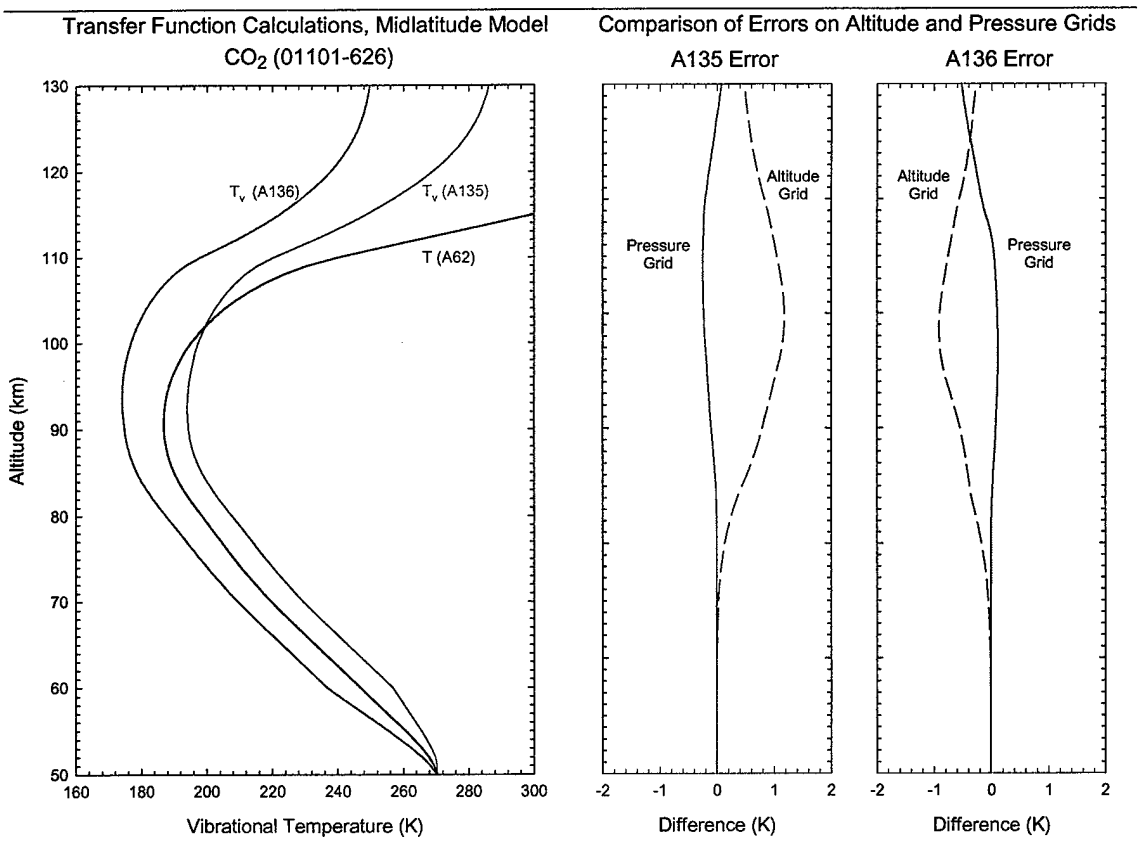

Figure 18. Transfer-function calculations for the CO_2 626 01101 vibrational temperature. On the right, errors resulting from the normal calculation ("altitude grid") are compared with those from the simulation ("pressure grid"). See the discussion in the text.

There is a notable improvement in the transfer-function results for this band when the "pressure grid" is used. What has happened is that the adjusted grid used for the perturbed atmospheres allows the column density in each individual layer to be nearly the same as what it was when the transfer functions were calculated originally. As a result, the $\overline{\tau}_\nu$ that are used when the LBL calculation is performed on the new grid are very close to what they were when the transfer functions were originally calculated. In contrast, when the fixed 1-km grid was used, the adjustments in pressure that accompanied the temperature perturbation produced an offset in these quantities. By adjusting the geometrical layer thickness, the simulation compensates for this offset.

The process of simulating a pressure grid is a tedious one since it requires a careful remapping of the atmospheric state vector for every perturbation that is made. The purpose of this exercise was to determine whether improvements could be made if the entire code were rewritten to use a pressure grid from the start. These results indicate that considerable improvement is possible, but we have not made enough tests to establish the range of conditions for which it would be helpful and worthwhile.

4. SABER

NASA's Thermosphere-Ionosphere-Mesosphere-Energetics and Dynamics (TIMED) satellite will provide extensive new data relating to the basic structure and energy budget of the mesosphere and lower thermosphere (MLT). Near-continuous measurements of different atmospheric emissions will provide a more complete and comprehensive survey of the relatively unexplored region between 60 and 180 km than has ever been obtained before. It will return global data on winds, thermal structure, and densities of major and minor atmospheric constituents, and the variability of all these. It will enable better calculations of the ways that energy is exchanged among the various reservoirs in this region. And it will provide a timely database for researchers to draw upon.

We have participated in planning and development activities relating to one of the TIMED instruments, SABER (which stands for Sounding of the Atmosphere using Broadband Emission Radiometry). Some of these activities are described in the paper [*Mertens et al, 2001*] comprising Appendix B of this report. The remainder of this section gives a summary of that work, and discusses additional work involving our non-LTE models that was performed as part of the SABER operational software validation process.

4.1 Temperature Retrieval

The most critical single measurement for this mission is that of atmospheric kinetic temperature. This will be provided mainly by SABER, which will detect IR and NIR emissions in ten broadband channels, including four CO_2 channels. The use of 15 μm limb measurements for kinetic temperature retrieval is a well-tested technique, but in the past it has been satisfactory only for altitudes up to about 70 km, near the lower end of the range of interest for TIMED. Extending the retrievals to 100 km and higher requires not only an instrument with superior sensitivity, which SABER will provide, but also a retrieval algorithm that takes into account two things that have been neglected in the past. These are the non-LTE nature of the 15 μm emission and the lack of complete mixing of CO_2 in the mesosphere and above.

Such an algorithm has been developed and tested with simulated data [*Mertens et al 2001*]. Its two main components are a forward radiance model for simulating the 15 μm radiance that is to be matched, and an inversion model that actually determines the sought-after atmospheric state vector. Calculation of CO_2 non-LTE vibrational populations is an integral part of the forward radiance model. Since the algorithm is iterative, this calculation must be done repeatedly. In fact, it is done not only for the bend-stretch states that produce the 15 μm emissions but also for the asymmetric stretch states emitting at 4.3 μm. The latter are used (in daytime, at least) to determine the CO_2 volume mixing ratio.

We have worked on the development of the forward radiance model, and later on its validation, using results from our Atmospheric Radiance Code (ARC). Details of how this is used in the retrieval algorithm are given in the paper by Mertens et al [*2001*] that is included in this report as Appendix B, so we will not elaborate upon it here. We will instead list our contributions to this process, with an explanation of the purpose of, and conclusions drawn from, each of them.

We worked on the optimal definition of the narrow 15 μm channel's bandpass. The purpose was to insure that the fraction of the detected limb radiance coming from the 626 01101 state be as large as possible, since this state is closer to LTE than any of the others. We calculated vibrational temperatures up to 160 km and limb radiances up to 130 km for a variety of climatologically-based temperature profiles. To keep the signal to noise ratio as high as possible and minimize the number of non-LTE bend-stretch states that had to be modeled, we found that, with precise cutoffs, a bandpass of 665 to 710 cm^{-1} would be ideal. This would eliminate all minor-isotope Q branches, but with the 50% power points uncertain by 2 to 5 wavenumbers due to manufacturing uncertainties, it would be necessary to back off to at least 660 cm^{-1} on the specification.

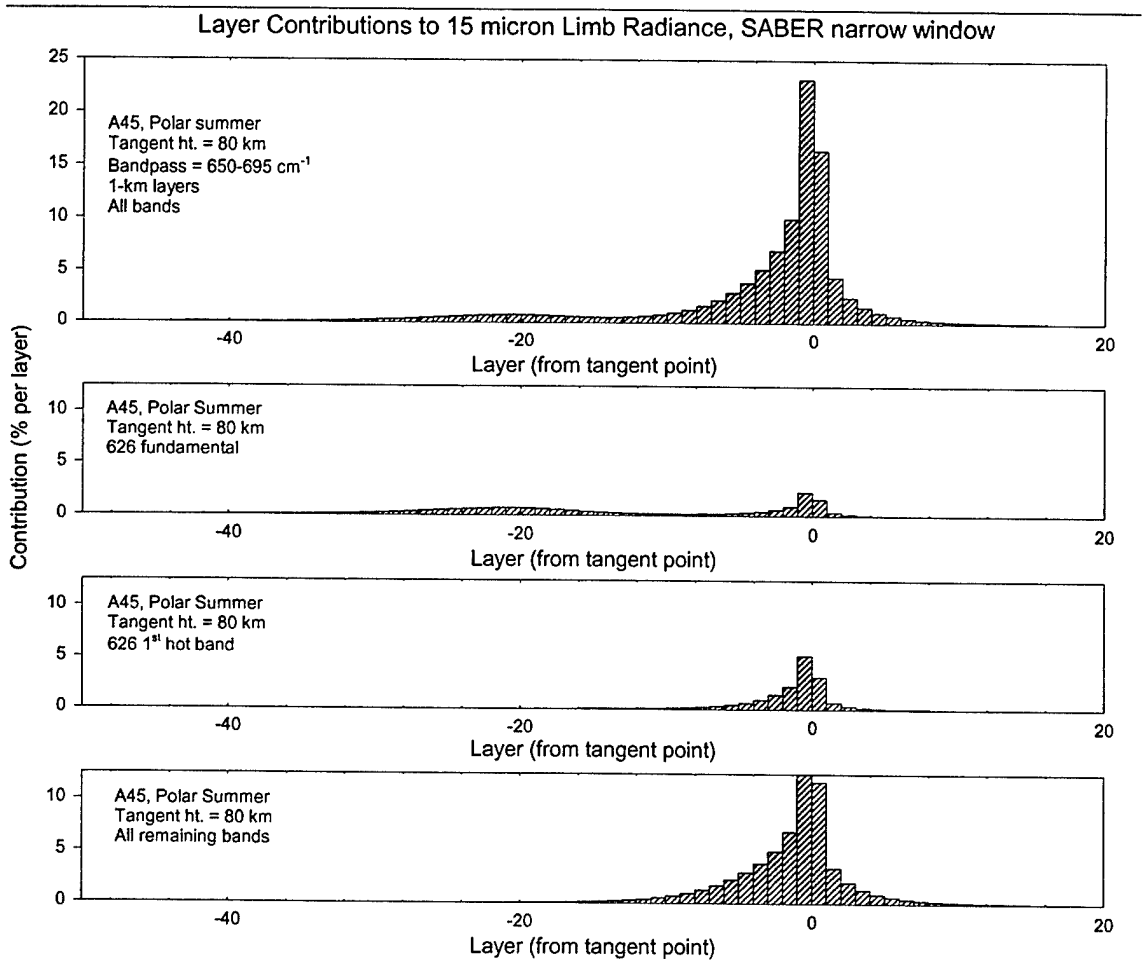

Figure 19. Layer contributions to the 15 μm emission within an idealized bandpass of 650-695 cm^{-1}, for a LOS with a tangent height of 80 km using a polar summer model atmosphere. The contributions are given as a percent of the total simulated radiance due to various combinations of bands. The layers were all 1 km thick vertically, and they are numbered according to their order along the LOS, with negative numbers identifying the layers nearer the observer and positive numbers indicating those on the far side of the tangent point. The subsidiary peak of the 626 fundamental near layer –20 comes from altitudes near 100 km.

We calculated the source regions for 15 μm limb radiance that would be observed and presented the information as plots of layer contributions. Figures 19 and 20 are examples showing, for a LOS with a tangent height of 80 km, fractions of the total observed limb radiance arising in the various layers between the observer and the tangent point, and beyond. They also break out the contributions from the ν_2 fundamental and other bands. The purpose was to evaluate the extent to which a bottom-up algorithm, as opposed to an onion-peel approach, would be suitable for retrieving kinetic temperature from such data. One can see that a substantial fraction of the emission in the 626 fundamental comes from layers much higher (~100 km), and closer to the observer, than the tangent point. We provided test model atmospheres that have been used for all the simulations and code validation procedures, and also the algorithm used for maintaining the proper concentrations of unmixed atmospheric constituents as the retrieved temperature/pressure profiles relax from their initial values to the final solution. The latter was based upon the simple specification of mixing ratios as a function of pressure rather than altitude; it was implemented in our code, CONST_PR.

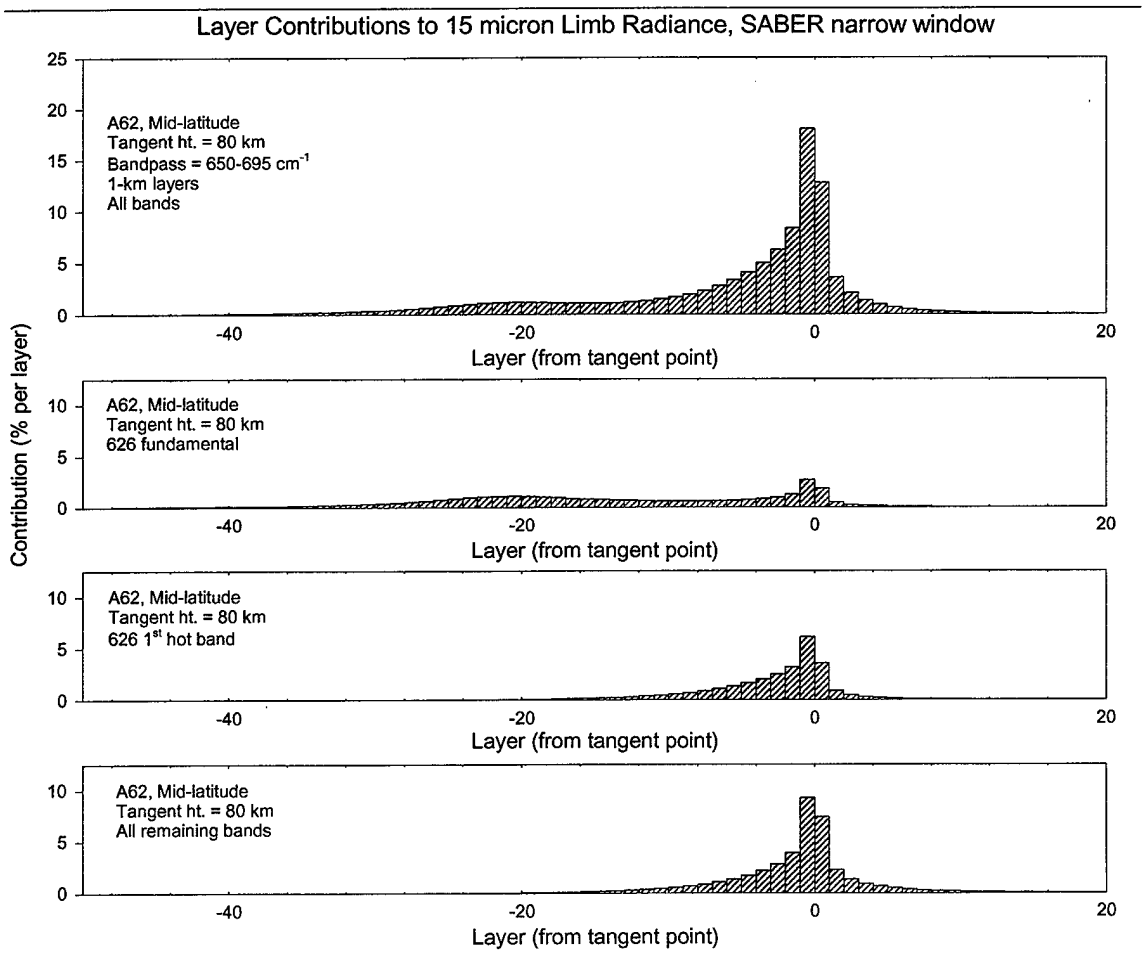

Figure 20. As Figure 19, but for a midlatitude model atmosphere.

We aided the validation of new algorithms in LINEPAK and BANDPAK enabling non-LTE calculations to be performed. LINEPAK is the LBL radiative transfer code used at NASA, and BANDPAK is the emissivity-growth band-model code for LOS radiance that has since been adapted for use in the SABER operational retrieval software. The greatest portion of our effort, however, involved validating the non-LTE forward model for CO_2 vibrational temperatures [e.g., *Wintersteiner et al, 2000a*]. The algorithm in the NASA operational software is based upon the Modified Curtis Matrix approach developed by Lopez-Puertas and co-workers at Instituto de Astrofisica de Andalucia (IAA) in Granada [e.g., *Lopez-Puertas et al, 1998a,b*]. Several years ago we validated the radiative-transfer algorithm in the IAA code by making detailed comparisons of its results for the bend-stretch states with those from our LBL code, RAD [*Lopez-Puertas et al, 1994*]. Since then there have been many improvements in both codes, and also there is now the need to validate the forward non-LTE model in the SABER operational code. That is needed not only for the bend-stretch states but also for the asymmetric stretch (4.3 μm) states, which are calculated because the operational code will derive CO_2 density. It will use SABER limb radiances from the 4.3 μm channel to do this, for daytime, in the region above 70 km where it appears not to be well-mixed.

Several objectives were satisfied by performing a three-way comparison using the ARC line-by-line code, the IAA Curtis Matrix code, and the new NASA code. One was to insure that the bend-stretch calculations in the first two of these still give the same results throughout the retrieval region, to check that the NASA code agrees as well, and to validate the daytime calculation for these states, which was previously ignored. Another was to validate the 4.3 μm radiative transfer calculation and check that all the important radiating states, including the Group 1 and Group 3 states, were correct, and consistent in the three codes. A part of the latter effort was a detailed consideration of all the processes that contribute to the production and loss of population in all these states. Finally, consideration was given to the proper way to iterate the calculations. That is necessary because none of the codes performs a fully-coupled calculation that simultaneously determines the populations of all the relevant states. Rather, populations of sets of states that depend upon each other are determined sequentially, so that it is necessary to calculate each set more than once. These results will be published in the future in one of several papers describing all the details of the algorithms and procedures to be used in the SABER data processing.

These exercises, which were quite extensive, led to improvements in both the benchmark ARC and IAA codes. They also showed that the new NASA code, although missing certain components at the time of the most recent tests, was giving correct results to the extent possible. Specifically, the bend-stretch states' vibrational temperatures from the NASA model were in agreement to those from ARC within less than 2 K up to 130 km for the cases that were run. In fact, some of that residual error was shown to be due to the 2-km layering imposed on the operational code by the instrument resolution; when 1-km layering was tried, the agreement was better and the calculation, presumably, more accurate. For the daytime asymmetric stretch states, agreement was also better than 2 K up to high altitudes, and actually better than 1 K up to at least 100 km.

They also showed that the basic production and loss mechanisms that have been incorporated into the 4.3 μm non-LTE models over the years [e.g., *Nebel et al, 1994; Lopez-*

Puertas et al, 1998a] are treated properly, and very likely comprise a set of processes sufficient to insure accurate modeling to within the sought-after 1 K. The lone exception was the treatment of the so-called laser bands, discussed below. These have been neglected in the past.

4.2 Laser Bands in the Daytime CO_2 Model

The laser bands connect the 00011 state with the 10002 and 10001 states, and produce emissions at 9.6 and 10.4 μm. The Einstein coefficients are on the order of 0.4 trans/(mol-sec), which is three orders of magnitude smaller than the 4.3 μm coefficients–the reason that radiative excitation and loss due to them had been neglected. The lines are almost all optically thin in the non-LTE region, however, whereas the 4.3 μm lines are strongly self-absorbed. As a result of trapping by the lines of the strong bands, in the mesosphere the loss rate due to emission in the weak bands is not negligible compared to the net production in the strong bands. Inclusion of loss in the laser bands alters the vibrational temperature of the 00011 state by as much as 3 K at some altitudes; clearly it plays a significant role [*Wintersteiner et at, 2000b*].

The question arose, if loss in these bands has such an effect, what about production? The difficulty in answering that question is that most of the radiative flux originates in the troposphere, where it is very difficult to model with non-LTE codes. The main reasons are cloud cover and line overlap. Cloud cover is completely unpredictable, but the upwelling flux with and without clouds is completely different since much of it arises in the lowest part of the atmosphere or at the ground boundary, where temperatures are much higher than at top-of-cloud altitudes. Even for clear skies, line overlap is a major complication as well. Non-LTE codes universally neglect it because it is generally unimportant at non-LTE altitudes and because of the computational burden it imposes. In our case, one of the laser bands overlaps the strong ozone ν_3 fundamental.

We studied the question by using FASE, the AFRL standard LBL radiance code, to determine the upwelling flux at altitudes in the mesosphere. We did this for a particular midlatitude clear-sky case with quite a warm ground boundary. We found that the radiance profile in each line was spectrally quite broad due to pressure-broadening in the lower atmosphere. In the mesosphere the line shape has a much smaller Lorentz component and so is much narrower. As a result, we were able to calculate the absorption rate in each line of the laser bands to quite a good approximation. That is, within several half-widths of the center of the narrow absorption profile the upwelling radiance was practically uniform, and although it varied from line to line it was possible to calculate the absorption in each line without using the full non-LTE code. The incremental production rate for 00011 due to the two laser bands was then determined by summing all these lines' contributions, so we put that into the non-LTE calculation and evaluated its effect.

Figure 21 shows the results of this exercise for daytime conditions using the midlatitude test case and a SZA of 60°. One can see in the left-hand panel that the addition of absorption due to upwelling flux is rather unimportant, producing differences on the order of 0.1 K. In the right-hand panel, the effect of neglecting laser-band processes entirely is obviously much greater. Moreover, because of the assumptions we made in doing this calculation (no clouds, warm ground boundary), the absorption rate should be near the upper limit for any scene. In view of the difficulties in modeling the upwelling

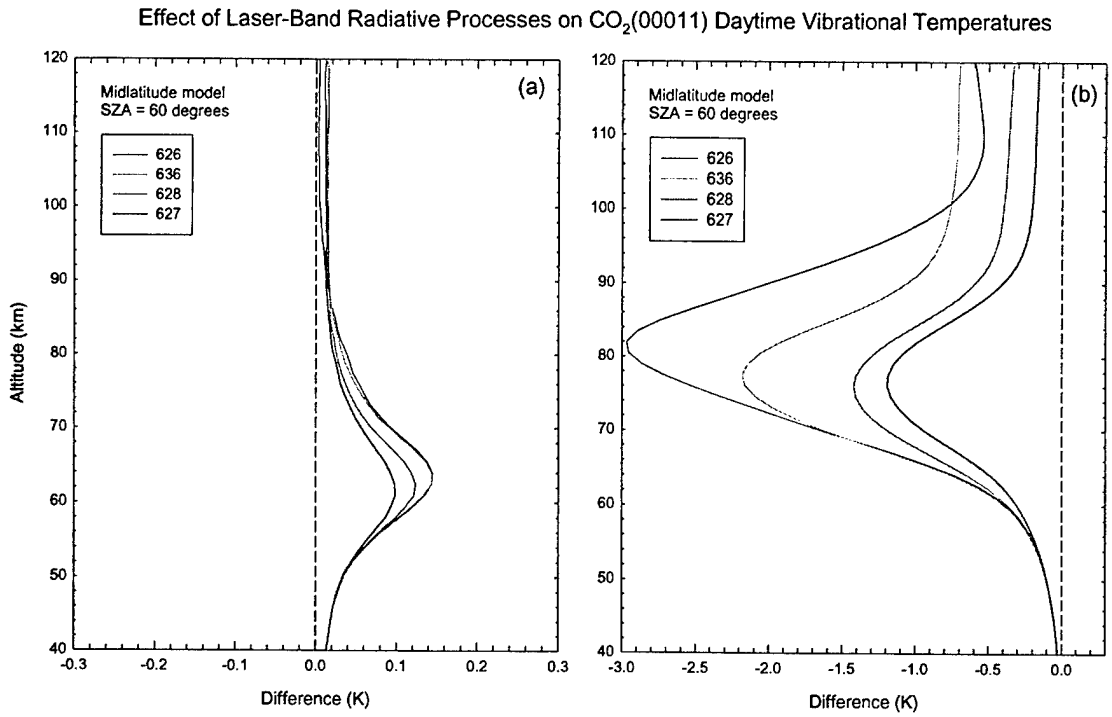

Figure 21. (a) The difference in the daytime 00011 vibrational temperatures, between the calculation assuming radiative excitation and loss in the laser bands, and that assuming radiative loss only, for the case discussed in the text. (b) The difference between the calculation assuming laser-band production and loss, and one assuming neither production nor loss. The lower vibrational temperature in (b) results from the calculation assuming that both laser-band processes contribute, since the loss is the greater of the two.

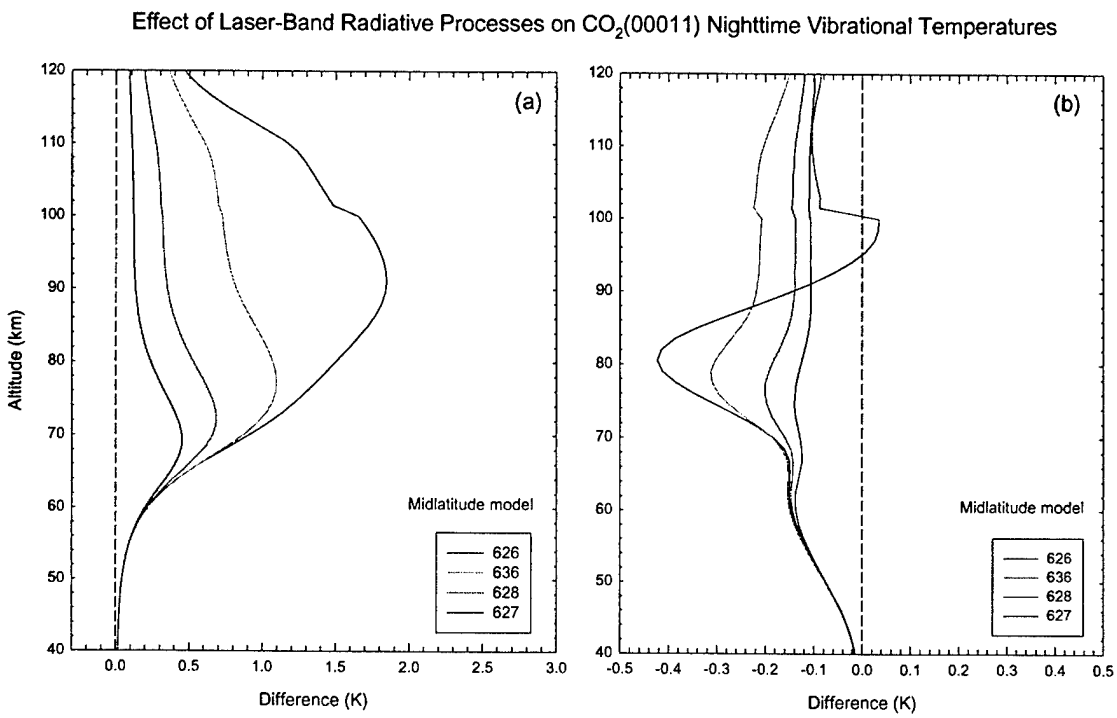

Figure 22. As Figure 21, but for nighttime conditions.

flux, it was easy to decide to neglect its effects in the SABER software and in the benchmark models.

Nighttime conditions present a somewhat more difficult choice, because the absence of solar excitation in the 4.3 μm bands leads to much lower vibrational temperatures for 00011. The loss rates in the laser bands are still not negligible compared to the net loss in the strong bands, even though both are much smaller in absolute terms. However, the upwelling flux is hardly different from daytime, assuming the same general conditions prevail. In the case we studied, it turns out that the absorption of upwelling laser-band radiation is comparable to the loss in these bands at night. Figure 22 shows the results. One can see that a better result is obtained by neglecting the laser bands completely; for this particular case, the production very crudely balances the loss.

The problem this poses for SABER is minimal. The ν_3 model is not invoked for nighttime conditions since the signal in the 4.3 μm channel will be too small to use for determining the CO_2 volume mixing ratio. For very low-Sun conditions, however, or for terminator conditions, this may affect the retrievals to be attempted, probably quite modestly; but we have not done studies to quantify that.

For research models the nighttime problem may have to be addressed if 1 K accuracy is required for these states. Our nighttime simulation produced an absorption rate, which is difficult to calculate, that is comparable to the loss rate. So in this case a better result is obtained by neglecting the laser bands entirely, rather than including only the loss. But that absorption rate was an upper limit calculation; different assumptions would have led to lower production rates, perhaps negligible (as in daytime) compared to the loss. So the issue of how to treat the laser bands in general at night is still unresolved.

5. Summary

During the period covered by this contract, technical progress was achieved on several fronts related to the acquisition, and modeling, of structured atmospheric radiance data. The major advances are detailed in the technical sections of this report, Sections 2-4, and in the published papers that are reproduced as Appendices A and B. The work described in our Scientific Report of 22 October 1998, entitled "Modeling Infrared Glow above Thunderstorms", also falls into this category but has not been reviewed again here.

We have developed and exercised codes for extracting, processing, and displaying data from the MSX Spectrographic Imagers (SPIMs). These data are unique because of the combination of their very large spectral range (EUV to NIR), excellent spectral resolution, and extremely fine spatial and temporal resolution. They enable researchers to view localized atmospheric phenomena on fine scales, using many different emission features if necessary, or alternatively to get an overview of larger portions of the data set by taking suitable averages. In either case, the data comprise a rich compendium of atmospheric radiance measurements, and the codes provide access to the measurements and the means of looking at the variability and spatial structure contained in them.

We have performed calculations having to do with certain MWIR radiance structures in the stratosphere observed by MSX. These have been important for identifying the source of the structure as thunderstorms.

We have made advances in non-LTE modeling by implementing the transfer-function algorithms in Atmospheric Radiance Code (ARC), and have demonstrated improvements in the accuracy and speed of the calculations made using it. We have used ARC to model a variety of atmospheric phenomena, to evaluate the effect of certain physical processes (for example, radiative contributions of the CO_2 laser bands) on the emission rates in the mesosphere, and as a tool to determine favorable instrument configurations for SABER. We have also participated in the development of the first non-LTE kinetic temperature retrieval algorithm, and used ARC to validate operational software that will be used to process the SABER data and perform the retrievals. We are in the process of preparing two research papers describing some of this work, for submission to research journals.

We have made the more important codes that we have developed in the course of our work, including all the ARC codes, available to researchers at Air Force Research Laboratory. We have provided source code and various materials, including sample files and output data, relating to the use of these codes, and have also engaged in discussions about how best to use them and what further developments would be most advantageous.

6. References

Dao, P.D., R. Farley, X. Tao, and C.S. Gardner, Lidar Observations of the Temperature Profile between 25 and 103 km: Evidence of Strong Tidal Perturbations, *Geophys. Res. Lett.,* **22**, 2825-2828, 1995.

Dewan, E.M., R.H. Picard, R.R. O'Neil, H.A. Gardiner, J. Gibson, J.D. Mill, E. Richards, M. Kendra, and W. Gallery, MSX Satellite Observations of Thunderstorm-Generated Gravity Waves in Mid-Wave Infrared Images of the Upper Stratosphere, *Geophys. Res. Lett.,* **25**, 939-942, 1998.

López-Puertas, M., P.P. Wintersteiner, R.H. Picard, J.R. Winick, and R.D. Sharma, Comparison of Line-by-Line and Curtis Matrix Calculations for the Vibrational Temperatures and Radiative Cooling of the CO_2 15 μm Bands in the Middle and Upper Atmosphere, *J.Quant. Spectrosc. Radiat. Transfer*, **52**, 409-423, 1994.

López-Puertas, M., G. Zaragoza, M.A. López-Valverde, and F.W. Taylor, Non Local Thermodynamic Equilibrium (LTE) Atmospheric Limb Emission at 4.6 μm 1. An Update of the CO_2 Non-LTE Radiative Transfer Model, *J. Geophys. Res.*, **103**, 8499-8513, 1998a.

López-Puertas, M., G. Zaragoza, M.A. López-Valverde, and F.W. Taylor, Non Local Thermodynamic Equilibrium (LTE) Atmospheric Limb Emission at 4.6 μm 2. An Analysis of the Daytime Wideband Radiances as Measured by UARS Improved Stratospheric and Mesospheric Sounder, *J. Geophys. Res.*, **103**, 8515-8530, 1998b.

Mertens, C.J., M.G. Mlynczak, M. López-Puertas, P.P. Wintersteiner, R.H. Picard, J.R. Winick, L.L. Gordley, and J.M. Russell III, Retrieval of Mesospheric and Lower Thermospheric Kinetic Temperature from Measurements of CO_2 15 μm Earth Limb Emission under non-LTE Conditions, *Geophys. Res. Lett.*, **28**, 1391-1394, 2001.

Mill, J.D., R.R. O'Neil, S. Price, G.J. Romick, O.M. Uy, and E.M. Gaposchkin, Midcourse Space Experiment: Introduction to the Spacecraft, Instruments, and Scientific Objectives, *J. Spacecraft Rockets*, **31**, 900-907, 1994.

Nebel, H., P.P. Wintersteiner, R.H. Picard, J.R. Winick, and R.D. Sharma, CO_2 Non-LTE Radiative Excitation and Infrared Dayglow at 4.3 μm: Application to SPIRE Data, *J. Geophys. Res.*, **99**, 10409-10420, 1994.

Picard, R.H., R.R. O'Neil, H.A. Gardiner, J. Gibson, J.R. Winick, W.O. Gallery, A.T. Stair, Jr., P.P. Wintersteiner, E.R. Hegblom, and E. Richards, Remote Sensing of Discrete Stratospheric Gravity-Wave Structure at 4.3 μm from the MSX Satellite, *Geophys. Res. Lett.,* **25**, 2809-2812, 1998.

Sharma, R.D. R. O'Neil, H. Gardiner, J. Gibson, H. Dothe, J. Duff, P.P. Wintersteiner, and M. Kendra, MSX: Auroral Enhancement of Nitric Oxide LWIR Emission Observed by SPIRIT III Radiometer, *J. Geophys. Res.*, (accepted for publication, 2001).

Wintersteiner, P.P., R.H. Picard, R.D. Sharma, J.R. Winick, and R.A. Joseph, Line-by-Line Radiative Excitation Model for the Non-Equilibrium Atmosphere: Application to CO_2 15 μm Emission, *J. Geophys. Res.*, **97**, 18083-18117, 1992.

Wintersteiner, P.P., R.H. Picard, and J.R. Winick, Rapid non-LTE Calculations using the ARC Model, 5th SABER Science Team Meeting, NCAR, Boulder, CO, 22-23 February 1999(a).

Wintersteiner, P.P., R.H. Picard, and J.R. Winick, Improved Line-by-Line Infrared Radiative Transfer Algorithm for Non-LTE Modeling, 5th Colloquium on Atmospheric Spectroscopy Applications, Reims, France, 1-3 September 1999(b).

Wintersteiner, P.P., M. Lopez-Puertas, R.H. Picard, and J.R. Winick, Status of CO_2 Research Code Comparisons, 9th SABER Science Team Meeting, Hampton Univ., Hampton VA, 16-17 August, 2000(a).

Wintersteiner, P.P., J.R. Winick, and R.H. Picard, Summary of Calculations: Effect of Radiative Excitation in the CO_2 Laser Bands, 10th SABER Science Team Meeting, NCAR, Boulder, CO, 29-30 November 2000(b).

Appendix A

The paper by Picard et al [*1998*] that comprises Appendix A describes, in detail, work that was briefly summarized in Section 2.2 of this report.

GEOPHYSICAL RESEARCH LETTERS, VOL. 25, NO.15, PAGES 2809-2812, AUGUST 1, 1998

Remote sensing of discrete stratospheric gravity-wave structure at 4.3-μm from the MSX satellite

R. H. Picard,[1] R. R. O'Neil,[1] H. A. Gardiner,[1] J. Gibson,[1] J. R. Winick,[1] W. O. Gallery,[2] A. T. Stair, Jr.,[3] P. P. Wintersteiner,[4] E. R. Hegblom,[5] and E. Richards[5]

Abstract. Distinctive structure in the 4.3-μm spectral region has been imaged by the SPIRIT 3 radiometer on the MSX satellite observing the cloud-free atmosphere. We show nadir, high-nadir-angle (NA) sublimb, and limb images which, coupled with radiative transfer analysis, indicate that this structure originates from internal gravity waves (GWs). Such structure occurs in a significant fraction of both below-the-horizon (BTH), or sublimb, and above-the-horizon (ATH), or limb, observations in both MSX 4.3-μm channels. The structure has different morphology from clouds and has spatial scales appropriate for atmospheric GWs. Calculation of contribution functions (CFs), or weighting functions, for MSX filters and viewing conditions confirms that the BTH GW structure originates from altitudes near 40 km. We believe this is the first high-resolution imaging of atmospheric GWs from space in the mid-wave infrared (MWIR) spectral region. In addition, the technique provides structure imaging capabilities at upper stratospheric altitudes inaccessible to airglow imagery.

1. Introduction

The SPIRIT-3 radiometer on the MSX (Midcourse Space Experiment) satellite [*Mill et al.*, 1994; *O'Neil et al.*, 1994] has a MWIR focal plane array consisting of 192 elements in each of two staggered columns, providing a field-of-view (FOV) of 1°. In the near-circular MSX orbit at 900-km altitude individual pixels have resolutions of 80 m on the earth in nadir view, 190 m orthogonal to the line-of-sight (LOS) at the ground for 57° NA, and 310 m in the limb for stratospheric tangent heights (TH). The 4.3-μm CO_2 ν_3 B-band filter includes narrowband (B1, 4.22-4.36 μm) and wideband (B2, 4.24-4.45 μm) channels, each covering half of the total FOV. In one data-collection mode, the spacecraft looks at constant NA near 90° azimuth to the velocity vector, with the motion of the spacecraft (about 7 km/s) providing a "pushbroom" spatial scan.

[1]Air Force Research Laboratory, Hanscom AFB, Massachusetts

[2]Atmospheric and Environmental Research, Inc., Cambridge, Massachusetts

[3]Visidyne, Inc., Burlington, Massachusetts

[4]ARCON Corporation, Waltham, Massachusetts

[5]Boston College, Institute for Space Research, Newton, Massachusetts

Copyright 1998 by the American Geophysical Union.

Paper number 98GL01701.
0094-8534/98/98GL-01701$05.00

Between May 1996 and February 1997, a database of 230 such data collections was accumulated with approximately 80 BTH and 150 ATH collections. A large fraction of the data from both B1 and B2 channels shows evidence of distinct wavelike structure. We present evidence that this structure is due largely to GW near 40-km altitude. Additional arguments for the origin of the structure seen by MSX to be in stratospheric internal GWs are being presented elsewhere (*Dewan et al.* [1998] and J. H. Brown, private communication, 1997).

Prior observations of GW from space have been made in the ultraviolet (UV) [*Ross et al.*, 1992], visible-to-near-IR [*Hersé*, 1984; *Mende et al.*, 1994, 1997], long-wave IR [*Fetzer and Gille*, 1994], and millimeter-wave [*Wu and Waters*, 1996a,b] regions of the spectrum. The MSX observations differ in that they report, for the first time, high-resolution imagery of waves in the MWIR and at stratospheric altitudes near 40 km. By contrast, all previous observations except *Fetzer and Gille* [1994] and *Wu and Waters* [1996a,b] have measured airglow layers at 85-100 km in the UV to very near IR.

2. Observations

Figure 1a shows a nadir image of high-altitude cloud structure from the MSX B bands. It consists of a 34-s segment of data taken at 08:11 UT on 25 May 1996 over the China Sea. The detector array output is displayed vertically in Figure 1a (cross-scan direction) while time runs horizontally. The footprint velocity of 6.6 km/s can be used to convert time to spatial in-scan distance. The image then covers an area $\sim$ 15 km $\times$ 225 km. The top (bottom) portion of the figure shows B2 (B1) band data. There is distinct irregular structure consisting of cloudlike islands or blobs with scales of 20-50 km in the B2-band data, but essentially no structure in B1.

This structure contrasts with that of Figure 1b, showing 58 s of data taken at 57° NA (17 August 1996, 11:03 UT) over the Indian subcontinent and Tibet. This is a high NA, near the horizon (NA of horizon = 61.2°). The image has an area $\sim$ 125 km $\times$ 375 km and shows structure very different from Figure 1a: (1) The structure in the latter figure appears to be wavelike with scales of 15-50 km rather than cloudlike, and (2) it occurs in the B1 channel as well as the B2 channel. The contrast becomes even more striking if we take horizontal slices of the images at typical points in the B1 and B2 filter regions. The resulting pixel histories are shown in Figure 1c (1d) for the image of Figure 1a (1b). We see that the cloudlike structure corresponds to reductions, or "bite-outs", in the radiance profile, while the wave-

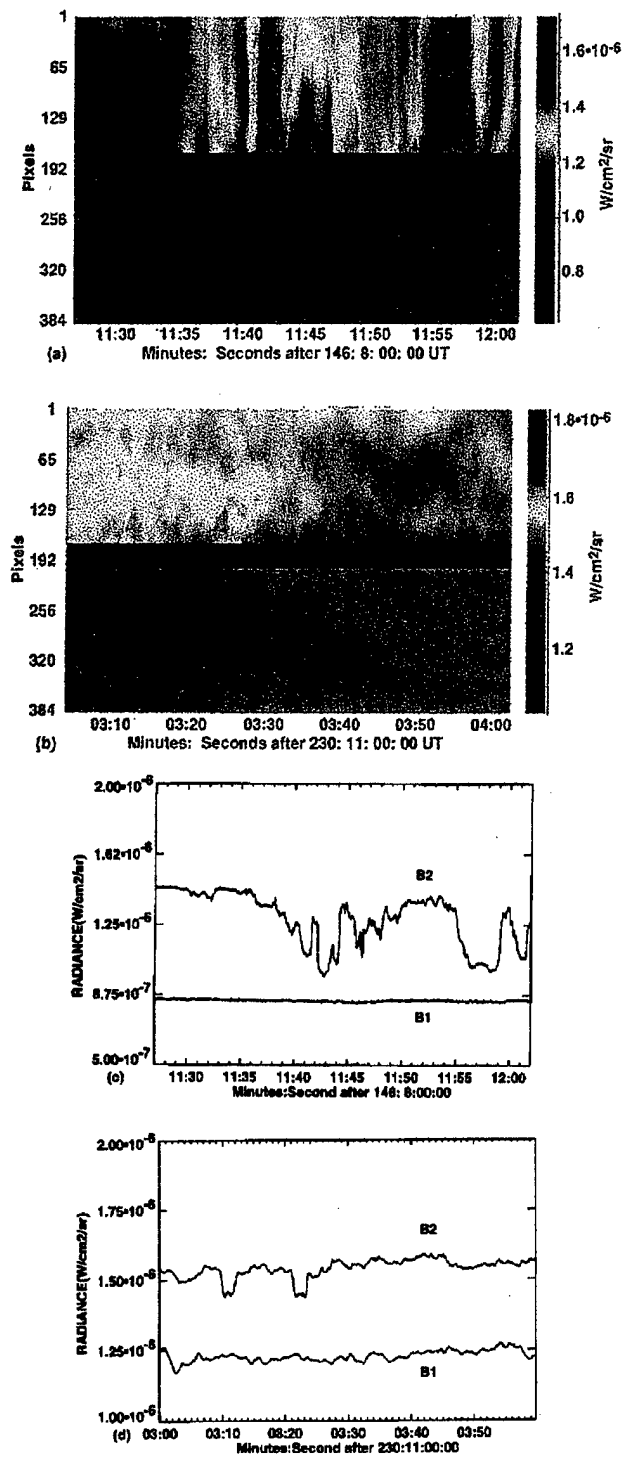

Figure 1. (a) Nadir image of high cloud structure from MSX 4.3-μm B bands, 25 May 1996. Narrow B1 (wide B2) filter band is at bottom (top) of image. (b) Image of wavelike structure at 57° NA, B1 and B2 bands, 17 August 1996. (c) Traces of typical B1 and B2 pixels for image in (a). (d) Same for image in (b).

like structure consists of symmetric fluctuations about a mean trend. The bite-outs occur in B1 only and are due to reduced radiance from cold high cloud tops. The wavelike structures appear to have a fractional radiance modulation of a few percent and are of similar strength in bands B1 and B2. This behavior is characteristic of all wavelike observations in the data set.

Discrete wavelike structures also appear in the ATH data set (Figure 2). This image (19 August 1996, 16:45 UT), depicts a 524 s pushbroom scan (~3000 km length) acquired at mid to high latitudes over the Pacific. The bottom B1 pixel is located almost exactly at the horizon, while the top B2 pixel has its TH near 60 km. The image shows wavelike modulation at a wide range of THs with scales of ~ 40-400 km superposed upon the expected sharp radiance gradient in the cross-scan (vertical) direction.

3. Radiative Transfer. Evidence for Gravity Waves

The apparent scales (15-50 km) of structure, in the BTH scan in particular, are too short to be due to planetary waves and too long to result from turbulence. However, the horizontal scales λ_x are consistent with GW horizontal scales (for example, [*Hines*, 1960]). We have tacitly assumed that any wave structure is "frozen-in" and does not change during the period of observation T. This is true in our BTH examples above since $T \ll \tau_b$, the Brunt-Vaisala period, while the wave period $\tau > \tau_b$. The latter restriction does not apply to the shorter-period infrasonic waves, which would not be frozen in our images, but are ruled out since they have much larger characteristic horizontal scales.

By calculating the CF for MSX SPIRIT 3, we can obtain further confirmation of the nature of the observed fluctuations. By CF, we mean the relative contribution of a volume element to the radiance at the sensor as a function of distance along the LOS or, alternatively, as a function of emitter altitude. The B-channel emission, arising from several 4.3-μm ν_3 bands of CO_2, is strongly self-absorbed. Hence, for a BTH LOS, the CF will not generally peak at the ground where the emitter density is maximum, but at finite altitude. Weaker isotopic and hot bands will be attenuated less than the main band and will be associated with CF peaks further from the sensor and at lower altitude.

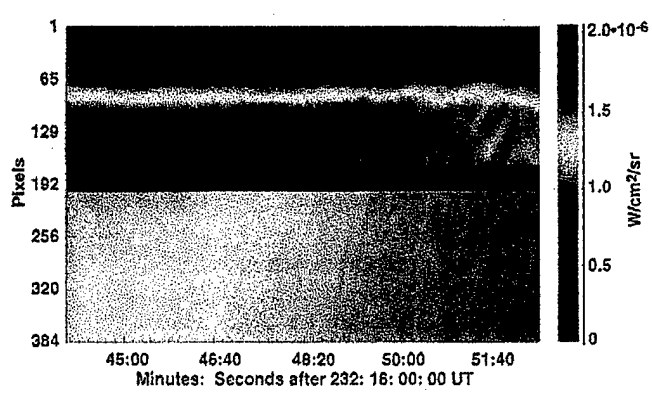

Figure 2. Limb image of 4.3-μm wavelike structure, B1 and B2 bands, 19 August 1996.

In Figure 3 we show the CF calculated for MSX conditions from the FASE line-by-line radiative-transfer code, evolved from FASCODE [*Clough et al.*, 1986]. The CFs of the top (center) images are calculated for MSX BTH LOS, for a NA of 0° (57°), appropriate to the data of Figure 1a (1b). The background atmosphere was generated by MSIS-90E [*Hedin*, 1991] for the locations and times of the images in Figure 1. In each case, the false-color image shows the spectral CF as a function of IR wavenumber ν and of altitude z for an instrumental spectral width of 2 cm^{-1}. The solid and dashed traces at the top show the corresponding total spectral radiances reaching the sensor as a function of ν. The main band of the most abundant isotope ($^{16}O^{12}C^{16}O$, or 626; band origin 2349 cm^{-1}) is strongly self-absorbed and peaks high in the stratosphere at an altitude of 40-45 km. The Q-branch of the 626 hot band is visible at 2337 cm^{-1} overlying the P-branch of the main band. At 2283 cm^{-1} on the red side of the main band a weaker ^{13}C isotopic band appears, peaking in the troposphere near 10 km, and features from even weaker bands are also visible in this region, including the hot band of the ^{13}C isotope (2272 cm^{-1}). Deviations from LTE (local thermodynamic equilibrium) are included through the ARC non-LTE code [*Wintersteiner et al.*, 1992; *Nebel et al.*, 1994] and account for some of the mesospheric features visible in the CF, but are not significant contributors to the radiance for BTH LOS.

Both B1 and B2 filters (Figure 3, bottom panel) have very steep edges resulting in high out-of-band rejection, and B2 has extended long-wave response encompassing the ^{13}C isotopic band. The CFs for the B1 and B2 channels, plotted versus z to the right of the images in Figure 3, are obtained by integrating the spectral CFs using the filter responses. The main peak of both B1 and B2 occurs near 40 km with a full width of 20 km, and both channels show a weak non-LTE peak near 80 km. In addition, B2 has a third prominent tropospheric peak largely due to the ^{13}C band (636). As the LOS moves from the nadir to the horizon, the CF peak altitude does not change, but the stratospheric peak narrows and the tropospheric peak diminishes in relative size. This behavior of the CF explains why wavelike perturbations are more evident at higher NA.

With these characteristics of the CFs, we can understand the images in Figure 1. The tropospheric cloud scene in Figure 1a does not appear in B1 because the B1 CF has little response below 30 km. However, B2 responds to clouds because of its extended red-side response, picking up the weaker ^{13}C tropospheric peak in the spectral CF. On the other hand, the wavelike scene

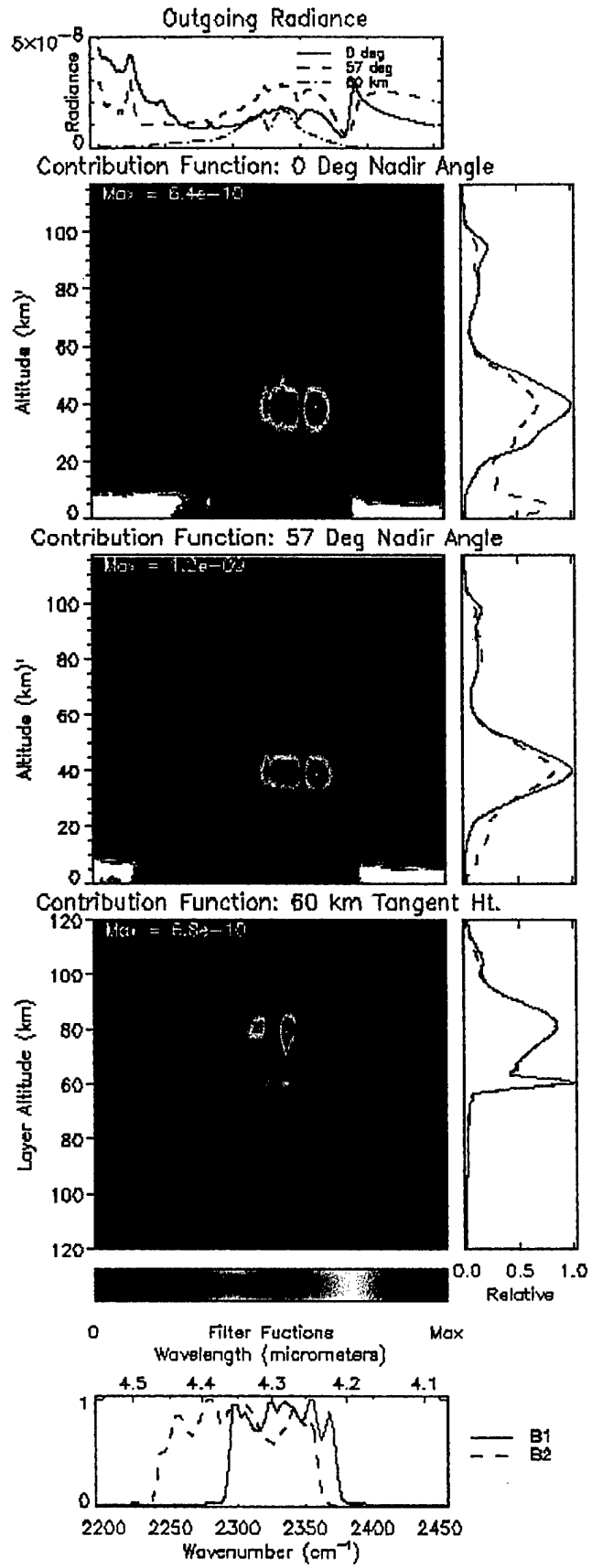

Figure 3. MSX spectral CFs (units - W/cm^2-sr-cm^{-1}-km^{-1}, or spectral radiance per unit altitude) for three cases: Top image – 0° NA, center image – 57° NA, bottom image – 60-km TH. Images are plotted at 2 cm^{-1} resolution versus wavenumber ν (horizontal) and altitude z (vertical). Color scale is linear with maximum value indicated on each image. Off-scale contributions are indicated in white. Traces to right of images show CF profiles for B1 and B2 versus z. Relative responses of B1 and B2 are shown in bottom graph, and top graph shows spectral radiances (W/cm^2-sr-cm^{-1}) at sensor as function of ν for all cases.

in Figure 1b shows modulation in both channels due to stratospheric GWs in the 40-km altitude range. The CF will act as a low-pass filter for GWs, filtering out waves with vertical (horizontal) wavelength much less than its width in height z (horizontal distance x). However, the horizontal filtering is anisotropic, since only waves with wave vectors aligned along the LOS are filtered out.

CFs can be calculated analogously for an ATH LOS. For optically thin emitters the CF will be symmetric in path length with maximum at the TH. When the emitter is optically very thick, as in this case, the CF becomes asymmetric and may have a primary or secondary peak nearer the sensor and above the TH. We display an ATH CF for a TH of 60 km (Figure 3, bottom image). The image is quite analogous to the BTH images, except for changes required by the limb geometry. The two volume elements along the LOS at the same altitude are shown symmetrically about the TH, which is at the center of the image, with the element nearer the sensor at the top. The CFs for filters B1 and B2 show the relative contributions to the total radiance per km of altitude for different elements along the LOS. There are no great differences between the two filters, as there were in the BTH case, since the strongest emitting features are well within the long-wave cutoff of filter B1.

As in the BTH case, the ATH response to GWs exhibits anisotropic spatial filtering of waves. Due to the large horizontal path at the TH, the horizontal filtering along the LOS can be quite severe, especially for THs near 40 km, where the tangent-point emission is dominant. At the 60-km TH shown in Figure 3, however, the tangent-point emission is no longer dominant and the broad response in altitude can lead to severe filtering of shorter vertical wavelengths.

4. Conclusions

We have shown considerable evidence that the discrete wavelike structures seen in both BTH and ATH MSX SPIRIT 3 images at 4.3 μm originate from stratospheric GWs. This has been accomplished partly by an analysis of the response of the narrow B1 and wide B2 filters and their corresponding CFs. We believe that this is the first remote imagery of GWs from space in the IR portion of the spectrum beyond 1 μm. In addition, we have recorded GWs near 40 km altitude where there are few prior passive space-based optical observations. Based on these results, special-purpose 4.3-μm spaceborne sensors could become an important new tool for investigating wave structure in the atmosphere. By using radiometers with narrower spectral bandpasses or an IR spectrometer with moderate resolution, one could tailor the location and shape of the CF peak, so that GW imaging at other altitudes could be possible.

Acknowledgments. MSX is sponsored by the Ballistic Missile Defense Organization. The support and encouragement of Maj. Peter Kurucz, Deputy Program Manager, and Dr. John D. Mill, Project Scientist, are gratefully acknowledged. The work of RHP, JRW, and PPW has been supported by the Air Force Office of Scientific Research. We are grateful to E. M. Dewan and J. H. Brown for many helpful discussions and to other members of the MSX Earthlimb Science Team for their useful comments and suggestions.

References

Clough, S. A., F. X. Kneizys, E. P. Shettle, and G. P. Anderson, Atmospheric radiance and transmittance: FASCOD2, *Sixth Conference on Atmospheric Radiation*, 141-144, American Meteorological Society, Boston, 1986.

Dewan, E. M., R. H. Picard, R. R. O'Neil, H. A. Gardiner, J. Gibson, J. D. Mill, E. Richards, M. Kendra, W. O. Gallery, MSX satellite observations of thunderstorm-generated gravity waves in mid-wave infrared images of the upper stratosphere, *Geophys. Res. Lett., 25*, 939-942 (+ cover), 1998.

Fetzer, E. J., and J. C. Gille, Gravity wave variance in LIMS temperatures. Part I, *J. Atmos. Sci., 51*, 2461-2483, 1994.

Hedin, A. E., Extension of the MSIS thermosphere model into the middle and lower atmosphere, *J. Geophys. Res., 96*, 1159, 1991.

Hersé, M., Waves in the OH emissive layer, *Science, 225*, 172-174, 1984.

Hines, C. O., Internal atmospheric gravity waves at ionospheric heights, *Can. J. Phys., 38*, 1441-1481, 1960.

Mende, S. B., G. R. Swenson, S. P. Geller, and K. A. Spear, Topside observation of gravity waves, *Geophys. Res. Lett., 21*, 2283-2286, 1994.

Mende, S. B., S. P. Geller, and G. R. Swenson, Gravity wave modulated airglow observation from spacecraft (abstract), *Eos Trans. AGU, 78*(17), Spring Meet. Suppl., S237, 1997.

Mill, J. D., R. R. O'Neil, S. Price, G. J. Romick, O. M. Uy, and E. M. Gaposchkin, G. C. Light, W. W. Moore, Jr., T. L. Murdock, and A. T. Stair, Jr., Midcourse Space Experiment, *J. Spacecraft Rockets, 31*, 900-907, 1994.

Nebel, H., P. P. Wintersteiner, R. H. Picard, J. R. Winick, and R. D. Sharma, CO_2 non-local thermodynamic equilibrium radiative excitation and infrared dayglow at 4.3 μm: Application to Spectral Infrared Rocket Experiment data, *J. Geophys. Res., 99*, 10409-10419, 1994.

O'Neil, R. R., H. A. B. Gardiner, J. Gibson, C. Humphrey, R. Hegblom, M. E. Fraser, M. Kendra, P. Wintersteiner, and C. Rice, Midcourse Space Experiment (MSX), *Proc. Soc. Photo. Opt. Instrum. Eng., 2223*(25) 264-273, 1994.

Ross, M. N., A. B. Christensen, C.-L. Meng, and J. F. Carbary, Structure in the UV nightglow observed from low earth orbit, *Geophys. Res. Lett., 19*, 985-988, 1992.

Wintersteiner, P. P., R. H. Picard, R. D. Sharma, J. R. Winick, and R. A. Joseph, Line-by-line radiative excitation model for the non-equilibrium atmosphere: Application to CO_2 15-μm emission, *J. Geophys. Res., 97*, 18083-18117, 1992.

Wu, D. L., and J. W. Waters, Gravity-wave-scale temperature fluctuations seen by the UARS MLS, *Geophys. Res. Lett., 23*, 3289-3292, 1996a.

Wu, D. L., and J. W. Waters, Satellite observations of atmospheric variances: A possible indication of gravity waves, *Geophys. Res. Lett., 23*, 3631-3634, 1996b.

W.O. Gallery, AER, Inc., 840 Memorial Drive, Cambridge, MA 02139

H.A. Gardiner, J. Gibson, R.R. O'Neil, R. H. Picard, and J. R. Winick, AFRL/VSBM, Hanscom AFB, MA 01731 (e-mail: picard@plh.af.mil)

E.R. Hegblom and E. Richards, Boston College, Institute for Space Research, Newton, MA 02159

A. T. Stair, Jr., Visidyne, Inc., 10 Corporate Place, S. Bedford Street, Burlington, MA 01803

P. P. Wintersteiner, ARCON Corporation, 260 Bear Hill Road, Waltham, MA 02154

(Received December 5, 1997; accepted March 6, 1998.)

Appendix B

The paper by Mertens et al [*2001*] that comprises Appendix B describes, in detail, work that was briefly summarized in Section 4.1 of this report.

GEOPHYSICAL RESEARCH LETTERS, VOL. 28, NO. 7, PAGES 1391-1394, APRIL 1, 2001

Retrieval of mesospheric and lower thermospheric kinetic temperature from measurements of CO_2 15 μm Earth limb emission under non-LTE conditions

Christopher J. Mertens,[1,2] Martin G. Mlynczak,[3] Manuel López-Puertas,[4] Peter P. Wintersteiner,[5] R. H. Picard,[6] Jeremy R. Winick,[6] Larry L. Gordley,[1] and James M. Russell III[7]

Abstract. We present a new algorithm for the retrieval of kinetic temperature in the terrestrial mesosphere and lower thermosphere from measurements of CO_2 15 μm earth limb emission. Non-local-thermodynamic-equilibrium (non-LTE) processes are rigorously included in the new algorithm, necessitated by the prospect of satellite-based limb radiance measurements to be made from the TIMED/SABER platform in the near future between 15 km and 120 km tangent altitude. The algorithm requires 20 seconds to retrieve temperature to better than 3 K accuracy on a desktop computer, easily enabling its use in operational processing of satellite data. We conclude this letter with a study of the sensitivity of the retrieved temperatures to parameters used in the non-LTE models, including sensitivity to the rate constant for physical quenching of CO_2 bending mode vibrations by atomic oxygen.

Introduction

Techniques to retrieve temperature profiles from broadband measurements of CO_2 15 μm earth limb emission from the middle atmosphere were developed more than 30 years ago (e.g., [*Gille and House*, 1971]). In these techniques a basic assumption was that carbon dioxide (CO_2) was well mixed and its volume mixing ratio (vmr) was well known. Another key assumption was that the observed CO_2 transitions were in LTE. These assumptions were sufficient for previous sensors whose sensitivity did not permit limb radiance measurements much above 70 km tangent height.

In the very near future, NASA will launch and commence operations of the Thermosphere-Ionosphere-Mesosphere Energetics and Dynamics (TIMED) mission whose primary goals are to measure the thermal structure and to quantify the energy budget of the 60-180 km region. One TIMED instrument, SABER (Sounding of the Atmosphere using Broadband Emission Radiometry), will measure CO_2 limb emission in the 15 μm spectral interval to approximately 120 km in altitude for the purpose of determining kinetic temperature (T_k). SABER is a broadband radiometer with 10 spectral channels ranging from 1.27 μm to 16 μm. To analyze the SABER limb radiance data in terms of T_k, new retrieval approaches must be developed to deal effectively with the occurrence of non-LTE in the observed vibration-rotation bands of CO_2 as well as variability in the CO_2 vmr. The purpose of this letter is to present the algorithm for retrieving T_k from non-LTE emission measurements and to present the sensitivity of the retrievals to parameters in the non-LTE model.

Temperature retrieval approach

Kinetic temperature is retrieved using SABER measured radiance from two CO_2 15 μm channels, a narrow bandpass channel (650-695 cm^{-1}) and a wide bandpass channel (580-760 cm^{-1}). The two CO_2 channels are used to register pressure with altitude in the stratosphere and infer T_k assuming LTE conditions. This approach is similar to the two-color technique of *Gille and House* [1971]. The LTE assumption breaks down in the mesosphere for the CO_2 15 μm bands. The non-LTE retrieval algorithm is then employed to infer T_k in the mesosphere and lower thermosphere (MLT) using measured radiance from the CO_2 narrow channel.

The LTE-retrieved T_k and pressure described in the preceding paragraph provide the lower boundary conditions for the non-LTE T_k retrieval. The lower boundary altitude is nominally taken to be 50 km.

The non-LTE T_k retrieval model is comprised of two main components: (1) the forward radiance model and (2) the inversion model. Moreover, the forward radiance

[1]G & A Technical Software, Newport News, Virginia
[2]Now at NASA Langley Research Center, Hampton, Virginia
[3]NASA Langley Research Center, Hampton, Virginia
[4]Instituto de Astrofisica de Andalucia, CSIC, Granada, Spain
[5]ARCON Corporation, Waltham, Massachusetts
[6]Air Force Research Laboratories, Space Vehicles Directorate, Hanscom AFB, Massachusetts
[7]Hampton University, Hampton, Virginia

Copyright 2001 by the American Geophysical Union.

Paper number 2000GL012189.
0094-8276/01/2000GL012189$05.00

model itself is composed of two parts: (1) the vibrational temperature (T_v) model and (2) the limb radiance model. Limb radiance is calculated using BANDPAK [*Marshall et al.*, 1994], now expanded for applications to non-LTE calculations. There are seventeen 15 μm bands that contribute to the limb radiance in the CO_2 narrow channel spectral bandpass. Vibrational temperatures for these seventeen bands are the non-LTE inputs into the limb radiance model. The non-LTE formulation in BANDPAK is a broadband extension of the line-by-line approach described by *Edwards et al.* [1993] and demonstrated by *Mlynczak et al.* [1994]. The vibrational temperatures are calculated from the operational CO_2 T_v model, which is a formulation of the Modified Curtis Matrix approach of *López-Puertas et al.* [1998a] that uses BANDPAK to perform all the radiation transfer calculations.

A number of techniques are used in the inversion model of the retrieval algorithm. There are two primary relaxation loops. In the inner loop a T_k profile is retrieved using the onion-peel approach while pressure and the T_v's are fixed. The onion-peel technique is characterized by first matching the emission of the outer atmospheric layer to the measured radiance, then successively matching the next inward layer. Kinetic temperature is retrieved at each tangent height by adjusting the local T_k until the modeled radiance matches the measured radiance within the convergence criterion. The temperature is adjusted using Newtonian iteration and the optimal estimation algorithm [*Rodgers*, 1976]. The inner loop convergence criterion is a requirement that the modeled radiance match the measured radiance within a user-specified fraction of the solution error (standard deviation).

The onion-peel approach is critical to retrievals in the mesosphere from the CO_2 15 μm bands since the limb radiance for mesospheric tangent heights is dominated by emission from higher altitude layers [*Wintersteiner et al.*, 1992]. The onion-peel technique ensures that the modeled emission matches the measured radiance from the upper altitude layers, even though the retrieved temperature-pressure combination may be incorrect at intermediate steps in the relaxation process. For a particular limb path, the effect is greater sensitivity to the local T_k at the sought-after tangent altitude.

Operationally, the *a priori* temperature profile for a particular measurement will be the retrieved temperature profile from the previous measurement. However, the *a priori* error variance is specified such that the solution error variance is dominated by measurement error (noise) over the range of altitudes where the signal-to-noise ratio is 10 or more. In effect, the weighting of *a priori* data is small over the altitude region where one can reasonably expect an accurate and precise retrieval from a direct measurement, and large enough outside of this altitude region to ensure a stable solution

In the outer relaxation loop, the pressure profile is rebuilt from the lower boundary using the onion-peel retrieved T_k profile and the barometric pressure law. The vibrational temperatures are updated using the CO_2 15 μm T_v model with the previously retrieved T_k and pressure profiles as input. The onion-peel retrieval (inner) loop is repeated until the entire inferred T_k profile relaxes within the convergence criterion, which is a requirement that the retrieved temperature profile differences between two successive onion-peel retrieval iterations be smaller than a user-specified fraction (same as above) of the solution error at a user-specified altitude. The user-specified altitude is chosen such that the signal-to-noise ratio is roughly 10 (typically, 110 to 115 km).

The top of the atmosphere (TOA) is nominally taken to be 140 km. This choice of TOA eliminates upper boundary effects on retrieved temperatures at altitudes where one can reasonably expect quality retrievals.

The non-LTE retrieval algorithm typically requires no more than five iterations in either (inner/outer) loop of the relaxation scheme. The algorithm can retrieve T_k at 51 tangent altitudes in 20 seconds on a desktop (500 Mhz Pentium) computer.

Results and Discussion

We now present retrieved temperature profiles from simulated SABER measurements and give estimates of the accuracy and sensitivity of the retrieved temperatures to parameters in the non-LTE model. The retrieval simulations were done on a 2 km grid, consistent with SABER's effective field-of-view. Shown in Figure 1 is a retrieval for a realistic temperature profile with two mesospheric inversion layers. This profile was derived from lidar measurements taken during the ALOHA 93 campaign [*Dao et al.*, 1995]. The first guess profile used to initialize the retrieval was an MSIS temperature profile, also shown in Figure 1. For the ALOHA case, the temperature profile is retrieved mostly within 3 K accu-

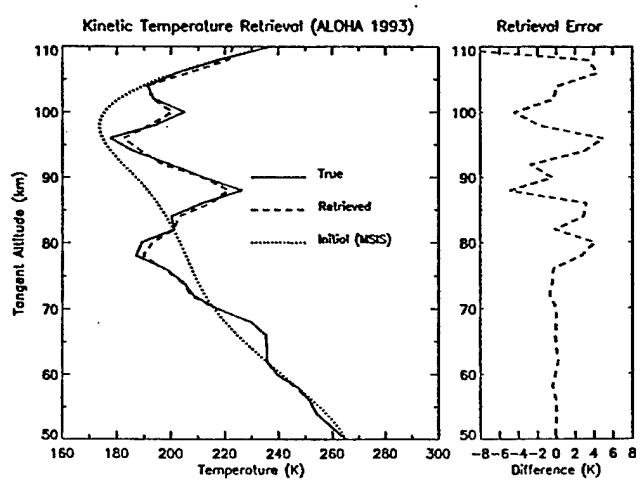

Figure 1. Simulated retrieval of kinetic temperature as measured by the SABER instrument for an atmosphere (ALOHA 93) with significant vertical structure.

Table 1. Determinations of k_o from laboratory measurements and as inferred from atmospheric observations

Laboratory Measurements			Atmospheric Observations	
Rate[a]	Temperature[b]	Reference	Rate[a]	Reference
1.4×10^{-12}	300	*Shved et al.* [1991]	6.0×10^{-12}	*Sharma and Wintersteiner* [1990]
1.2×10^{-12}	300	*Pollack et al.* [1993]	$3\text{-}6 \times 10^{-12}$	*López-Puertas et al.* [1992]
0.5×10^{-12}	301	*Lilenfeld* [1994]	1.5×10^{-12}	*Vollman et al.* [1997]

[a]Unit is $cm^{-3}s^{-1}$
[b]Unit is Kelvin

racy below 105 km, with the exceptions of a $\sim$ 5 K error at 88 and 96 km and a $\sim$ 4 K error at 80 and 100 km. Note also in Figure 1 the initial guess MSIS temperature profile has no small-scale atmospheric structure and differs from the lidar ("true") temperature profile by more than 35 K at some altitudes.

In the retrieval simulations presented above, the only sources of uncertainty included are simulated random instrument noise and calibration errors. There are other uncertainties to consider in a retrieval under non-LTE conditions. Specifically, CO_2 is apparently not well mixed above 75 km [*López-Puertas et al.*, 1998b]. Uncertainties in CO_2 will manifest themselves as uncertainties in the retrieved mesospheric temperature. In addition, uncertainties in the kinetic and spectroscopic parameters used in the computation of CO_2 T_v's will also contribute to uncertainties in the retrieved T_k. Certainly the most important of these parameters is the rate of physical quenching of CO_2 vibrations by collisions with atomic oxygen through the process

$$CO_2(01^10) + O \xrightarrow{k_o} CO_2(00^00) + O + 667\ cm^{-1}. \quad (1)$$

This process is critical to determining the T_v of the CO_2 ν_2 fundamental band in the upper mesosphere and lower thermosphere. The retrieved temperature profile depends on knowing the rate coefficient for this process (which we will call k_o) and the atomic oxygen concentration. There have been several determinations of k_o from which the rate has been inferred. The reported rate coefficients span the range from 0.5×10^{-12} cm^3s^{-1} at 301 K determined by *Lilenfeld* [1994] to 6×10^{-12} cm^3s^{-1} at 300 K inferred by *Sharma and Wintersteiner* [1990]. Table 1 lists the published values of the determinations of k_o. The temperature dependence of k_o is not known from laboratory measurement.

For the following sensitivity studies, we assume a 50% uncertainty in atomic oxygen and in k_o. We note that the SABER experiment will simultaneously measure the CO_2 abundance and that a number of techniques will be used to infer the atomic oxygen concentration (e.g.,

Table 2. Uncertainties in retrieved kinetic temperature (K) due to the specified uncertainty in the rate of physical quenching (k_o) of CO_2 vibrations by atomic oxygen (or equivalently, to uncertainty in atomic oxygen concentration) and due to the uncertainty in the CO_2 concentration (as described in the text). The uncertainty due to random instrument noise is in the column labeled "Noise". The column labeled "Cal" denotes the radiometric calibration error. The column "Total" is the root-sum-square of the uncertainty due to the previous 5 columns.

		Retrieval Uncertainty (K)					
Z(km)	T(K)	k_o(+50%) or [O]	k_o(-50%) or [O]	[CO_2]	Noise	Cal(1.7%)	Total
110.0	240.0	-7.4	16.3	7.6	11.3	-0.3	22.5
108.0	223.2	-6.0	14.2	4.5	6.9	0.1	17.5
106.0	212.8	-4.9	12.1	2.1	4.4	0.3	13.9
104.0	205.3	-3.9	10.0	0.8	5.7	0.4	12.2
102.0	199.5	-3.1	8.1	0.8	4.5	0.3	9.8
100.0	195.0	-2.4	6.4	1.4	3.5	0.2	7.8
98.0	191.7	-1.8	4.9	2.2	2.1	0.2	6.0
96.0	189.3	-1.2	3.6	2.9	2.6	0.2	5.4
94.0	187.7	-0.7	2.4	3.4	2.1	0.2	4.7
92.0	186.9	-0.3	1.4	3.6	1.4	0.2	4.1
90.0	186.8	-0.1	0.8	3.6	1.8	0.2	4.1
88.0	187.4	0.1	0.4	3.4	1.8	0.3	3.9
86.0	188.9	0.1	0.1	3.1	1.3	0.3	3.4
84.0	191.4	0.1	0.1	2.6	1.1	0.4	2.9
82.0	194.7	0.1	0.0	1.9	0.6	0.4	2.0
80.0	198.6	0.0	0.1	1.3	0.4	0.4	1.4

[*Mlynczak*, 1995]). The uncertainty in CO_2 is represented using two different CO_2 vmr profiles. The "true" CO_2 profile is assumed to be the profile taken from a rocket measurement described by *Wintersteiner et al.* [1992]. Temperature was retrieved using a CO_2 profile derived from ISAMS measurements [*López-Puertas et al.*, 1998b]. The two CO_2 profiles differ from one another between 70 and 110 km, with a maximum difference of $\sim$ 15% at 95 km. Shown in Table 2 are the results of this sensitivity study for a smoothed version of the US Standard Atmosphere. A goal of the SABER experiment from the outset has been to retrieve temperature to better than 3 K below 100 km in order to compute accurately the energy balance and dynamics of the mesosphere. Uncertainty in CO_2 dominates the error in retrieved temperature below 100 km. However, if the CO_2 abundance is simultaneously retrieved with sufficient accuracy, then uncertainties in atomic oxygen and k_o on the order of 50% or greater start to affect our ability to meet the SABER retrieval-uncertainty goal above about 90 km. In contrast, recall the order-of-magnitude range in the reported values for k_o. This goal can be achieved if the instrument performs on orbit as calibrated in the laboratory and if the non-LTE model and atmospheric parameters are known to accuracies better than indicated in Table 2.

Summary

We have presented an overview of a new algorithm for the rapid and accurate retrieval of T_k from measurements of CO_2 15 μm earth limb emission under non-LTE conditions. The algorithm faithfully recovers atmospheric temperature to better than 3 K accuracy for realistic atmospheres and runs in approximately 20 seconds on desktop computer hardware.

We note that in order to realize the potential of this algorithm (and hence, the SABER experiment) the range of uncertainty in k_o must be significantly reduced. We recommend a critical evaluation of the extant determinations by the chemical kinetics community. It would also seem prudent to quantify the dependence of this rate coefficient on temperature over the range commonly encountered in the MLT.

Acknowledgments. M.L-P. has been partially supported by CICYT under contracts ESP97-1798 and ESP97-1773-CO3-01. RHP and JRW are grateful to Kent Miller and to Paul Bellaire of the Air Force Office of Scientific Research for partial support of this work. The work of PPW was carried out under contract to Air Force Research Laboratories under contract F19628-96-C-0048. All authors acknowledge support from NASA Langley under its SABER project.

References

Dao, P. D., R. Farley, X. Tao, and C. S. Gardner, Lidar observations of the temperature profile between 25 and 103km: evidence of strong tidal perturbation, *Geophys. Res. Lett.*, *22*, 2825-2828, 1995.

Edwards, D. P., M. López-Puertas, and M. A. López-Valverde, Non-LTE thermodynamic equilibrium studies of the 15-μm bands of CO_2 for atmospheric remote sensing, *J. Geophys. Res.*, *98*, 14,955-14,977, 1993.

Gille, J. C., and F. B. House, On the inversion of limb radiance measurements. I: Temperature and thickness, *J. Atmos. Sci.*, *28*, 1427-1442, 1971.

Lilenfeld, H. V., Deactivation of vibrationally-excited *NO* and CO_2 by *O*-atoms, *Tech. Rept. PL-TR-94-2180, 28pp.*, Air Force Phillips Lab., Bedford, Mass., 1994.

López-Puertas, M., G. Zaragoza, M. A. López-Valverde, and F. W. Taylor, Non local thermodynamic equilibrium (LTE) atmospheric limb emission at 4.6 μm. 1. An update of the CO_2 non-LTE radiative transfer model, *J. Geophys. Res.*, *103*, 8499-8513, 1998a.

López-Puertas, M., G. Zaragoza, M. A. López-Valverde, and F. W. Taylor, Non local thermodynamic equilibrium (LTE) atmospheric limb emission at 4.6 μm. 2. An analysis of the daytime wideband radiances as measured by UARS Improved Stratospheric And Mesospheric Sounder, *J. Geophys. Res.*, *103*, 8515-8530, 1998b.

López-Puertas, M., M. A. López-Valverde, C. P. Rinsland, and M. R. Gunson, Analysis of the upper atmosphere CO_2 (ν_2) vibrational temperatures retrieved from ATMOS/Spacelab 3 observations, *J. Geophys. Res.*, *97*, 20,469-20,478, 1992.

Marshall, B. T., L. L. Gordley, and D. A. Chu, BANDPAK: Algorithms for modeling broadband transmission and radiance, *J. Quant. Spectrsc. Radiat. Transfer*, *52*, 581-599, 1994.

Mlynczak, M.G., Energetics of the middle atmosphere: Theory and observation requirements, *Adv. Space Res.*, *17*, 117-126, 1995.

Mlynczak, M. G., D. S. Olander, and M. López-Puertas. Rapid computation of spectrally integrated non-LTE limb emission, *J. Geophys. Res.*, *99*, 25,761-25,772, 1994.

Pollack, D. S., G. B. I. Scott, and L. F. Phillips, Rate constant for quenching of CO_2(010) by atomic oxygen, *Geophys. Res. Lett.*, *20*, 727-729, 1993.

Rodgers, C. D., Retrieval of atmospheric temperature and composition from remote measurements of thermal radiation, *Rev. Geophys. Space Phys.*, *14*, 609-624, 1976.

Sharma, R. D., and P. P. Wintersteiner, Role of carbon dioxide in cooling planetary atmospheres, *Geophys. Res. Lett.*, *17*, 2201-2204, 1990.

Shved, G. M., L. E. Khvorostovskaya, I. Yu. Potekhin, A. I. Dem'Ryanikov, A. A. Kutepov, and V. I. Fomichev, Measurement of the quenching rate constant of CO_2(0110)-*O* collisions and its significance for the thermal regime and radiation in the lower thermosphere, *Atmos. Ocean. Phys.*, *27*, 295, 1991.

Vollman, K., and K. U. Grossman, Excitation of 4.3 μm CO_2 emissions by $O(^1D)$ during twilight, *Adv. Space Res.*, *20*, 1185-1189, 1997.

Wintersteiner, P. P., R. H. Picard, R. D. Sharma, J. R. Winick, and R. A. Joseph, Line-by-line radiative excitation model for the non-equilibrium atmosphere: Application to CO_2 15-μm emission, *J. Geophys. Res.*, *97*, 18,083-18,117, 1992.

C. J. Mertens, NASA Langley Research Center, Atmospheric Sciences Competency, 21 Langley Boulevard, Mail Stop 401B, Hampton VA 23681-2199. (email: c.j.mertens@larc.nasa.gov)

(Received August 9, 2000; revised December 13, 2000; accepted December 14, 2000.)